CELL-SCALE MEASUREMENTS OF TISSUE VISCOELASTICITY USING THERMOREPONSIVE MECHANOSENSORS IN ENGINEERED TUMOR MODELS

Benjamin Campbell
Department of Chemical Engineering
McGill University, Montreal
February 2023

A thesis submitted to McGill University in partial fulfillment of the requirements of the degree of Master of Science in Chemical Engineering (Thesis)

Abstract

Matrix stiffness has been extensively investigated as a driver of cell behaviors and determinant of cell fates. These studies focused on cells cultured on linear elastic substrates, however the cellular microenvironment is not linearly elastic. A more accurate characterisation of tissues is as a viscoelastic material where there is a time dependence to relating stress and strain. Individual cells use traction forces to gauge their local mechanical environment and they have been shown to respond to viscous changes in their environment, independent of changes in elasticity. With individual cells being responsive to viscous changes and tissues being well characterised by viscoelasticity, it follows that understanding local cell-scale viscoelasticity of tissues could inform our understanding of tissue development and disease progression. However, few techniques exist capable of making such measurements, so it is unclear what the local viscoelastic properties which cells create and respond to are.

Here, we adapted the use of fluorescently labelled swellable mechanosensors to characterize microscale viscoelasticity within complex 3D tissues. These cell-sized sensors were previously used to measure local stiffness based on equilibrated sensor size changes. To further the technology for viscoelastic measurements, we characterized sensor generated stress in phantom tissues of prescribed elasticity. We then used the stress-sensor expansion curve in inverse finite element simulations to fit model strain-time curves with experimentally obtained strain-time curves from sensors embedded in tissues. As a first application, we evaluated the viscoelastic properties of invasive and non-invasive cancer tumor models and demonstrate a significant difference in viscous behavior at the cellular length scale within these realistic tissue models. This

technique provides the means to characterize viscoelasticity with cell-scale resolution at unprecedented tissue depths which supports future investigation of how mechanical characteristics of the local mechanical environment influence cell behavior.

Resumé

La rigidité de la matrice a fait l'objet d'études approfondies en tant que moteur du comportement des cellules et déterminant de leur devenir. Ces études se sont concentrées sur des cellules cultivées sur des substrats élastiques linéaires, mais le micro-environnement cellulaire n'est pas linéairement élastique. Une caractérisation plus précise des tissus est qu'il s'agit d'un matériau viscoélastique où la relation entre la contrainte et la déformation dépend d'un dixième de degré. Les cellules individuelles utilisent les forces de traction pour évaluer leur environnement mécanique local et il a été démontré qu'elles répondent aux changements visqueux de leur environnement indépendamment des changements d'élasticité. Les cellules individuelles étant sensibles aux changements visqueux et les tissus étant bien caractérisés par leur viscoélasticité, il s'ensuit que la compréhension de la viscoélasticité locale des tissus à l'échelle cellulaire pourrait nous aider à comprendre le développement des tissus et la progression des maladies. Cependant, il existe peu de techniques capables d'effectuer de telles mesures, et on ne sait donc pas quelles sont les propriétés viscoélastiques locales que les cellules créent et auxquelles elles répondent.

Ici, nous avons adapté l'utilisation de mécanocapteurs gonflables marqués par fluorescence pour caractériser la viscoélasticité à micro-échelle dans des tissus 3D complexes. Ces capteurs de la taille d'une cellule étaient auparavant utilisés pour mesurer la rigidité locale sur la base des changements de taille du capteur en équilibre. Pour faire progresser la technologie des mesures viscoélastiques, nous avons caractérisé la contrainte générée par le capteur dans des tissus fantômes d'une élasticité prescrite. Nous avons ensuite utilisé la courbe d'expansion contrainte-capteur dans des simulations inverses par éléments finis pour ajuster les courbes de déformation-temps du modèle aux courbes de déformation-temps obtenues expérimentalement

à partir de capteurs intégrés dans des tissus. Dans une première application, nous avons évalué les propriétés viscoélastiques de modèles de tumeurs cancéreuses invasives et non invasives et démontré une différence significative dans le comportement visqueux à l'échelle de la cellule dans ces modèles de tissus réalistes. Cette technique permet de caractériser la viscoélasticité avec une résolution à l'échelle cellulaire à des profondeurs tissulaires sans précédent, ce qui favorise les recherches futures sur la façon dont les caractéristiques mécaniques de l'environnement local influencent le comportement cellulaire.

Acknowledgements

I first want to thank my supervisor Prof. Chris Moraes. My joining the lab was largely due to your incredible passion for teaching and after only a couple of lectures in fluid mechanics, I knew that you were the type of person I would like to work with. You then allowed me to join the lab as an undergraduate the following semester and through the summer which got me hooked on research. While those 8 months didn't exactly go as planned with the onset of the pandemic, it ultimately planted the seed in my head to continue into graduate school. Then when nearing the end of my degree and not being sure what I was going to do after, you reached out to me, and I quickly committed to starting a masters under your supervision. It is hard to believe that it has been 3 years since I first started in the lab, but I have no regrets that everything happened this way and I am extremely grateful for your guidance and support throughout this time.

To all my lab mates, you have all been so incredibly welcoming and supportive. Steph and Nikita, thank you so much for taking me under you wings as an undergraduate and guiding me into doing real research. I've come a long way since I initially joined and that is in big part due to you two. Christina and Camille, thank you for all the cell culture training, advice on experiments, general lab chats and keeping the 7th floor lab running. Nick and James, thank you for all the food/drinks, games of squash, and gym sessions. Karthick and Chen, thank you for all the 4th floor microfabrication and 3D printing training/advice. Scott, thank you for all the help with fixing my spaghetti code, guiding me through image processing and teaching me the glory of MATLAB.

To Robert, Eric, and Ryan, thank you for being there to chat late at night and take my mind off lab work at the end of the week.

And last but not least, thank you Mom and Dad for you unwavering support, it is the reason I've been able to pursue my interests and follow my dreams.

Contribution of Authors

The data and analysis presented in this work was obtained by the author. Project conceptualization was developed by Prof. Chris Moraes and Stephanie Mok. Ph.D. Experiment design was jointly completed by the author, Prof. Chris Moraes and Stephanie Mok, Ph.D. Writing of the thesis was completed by the author with Prof. Chris Moraes kindly aiding in editing.

Table of Contents

List of Figures ..... *x*

List of Tables ..... *xi*

List of Abbreviations ..... *xi*

1. Introduction *1*

1.1 Motivation **1**

1.2 Aims **2**

2. Background *4*

2.1 Basics of mechanical properties **5**

2.2 Static vs dynamic moduli **7**

2.3 Challenges in measuring tissue mechanical properties **8**

2.4 Techniques for tissue mechanical property measurement **8**

2.4.1 Bulk measurement techniques 9

2.4.2 Surface measurement techniques 11

2.4.3 Internal measurement techniques 13

2.5 Viscoelastic modelling **16**

2.6 Mechanical properties as an indicator of breast cancer presence and progression **18**

2.7 Future Direction of the Field **21**

3. Approach *23*

4. Materials and Methods *26*

4.1 Sensor fabrication **26**

4.2 Polyacrylamide phantoms and rheology **30**

4.3 Tissue culture **31**

4.4 Micropocket spheroid formation **31**

4.5 Cold shock experiments **33**

4.6 Finite element modelling **33**

5. Results *37*

5.1 Bead expansion time dynamics **37**

5.2 Sensor calibration **38**

5.3 Stiffening and dissipation of viscous properties due to tissue fixation **42**

5.4 Comparing viscoelasticity in spheroids from cell lines of distinct invasiveness **43**

5.5 Evaluating local changes in viscoelasticity from induced invasive transitions **44**

6. Discussion *46*
6.1 Sensor calibration 46
6.2 Model assumptions 47
6.3 Imaging Challenges 48
6.4 Temperature control within tissues 49
6.5 Length of sensor expansion experiments 50
6.6 Changes in viscous properties of invasive tissues 50
7. Future Directions *53*
8. Conclusion *55*
9. References *57*

List of Figures

Figure 1: Publication in PubMed with the keyword 'Tissue Viscoelasticity' by year. 5
Figure 2: Basics of mechanical properties – Young's modulus. 6
Figure 3: Basics of mechanical properties – shear modulus. 7
Figure 4: Bulk mechanical property measurement of tissues. 9
Figure 5: Surface mechanical property measurement of tissues 11
Figure 6: Internal mechanical property measurement techniques 14
Figure 7: Common constitutive models for viscoelastic creep and stress relaxation 17
Figure 8: pNiPAAm sensors initial use in residual stiffness measurement 24
Figure 9: Schematic of pNiPAAm sensor fabrication 26
Figure 10: Sensor oil-water emulsion technique 28
Figure 11: Stain of collagen coating and compacted sensor size distribution 29
Figure 12: Micropocket device fabrication methodology 32
Figure 14: Model geometry 34
Figure 15: Model boundary conditions and meshing. 35
Figure 16: Sample experimental data processed by COMSOL interpolation function 36
Figure 13: Sensor expansion in weakly constraining matrix 37
Figure 17: Modelled stress-strain-sensor size-matrix stiffness relationship 38
Figure 18: Shear Rheology of polyacrylamide phantoms 39
Figure 19: Deviation from mean expansion ratio for sensors in phantom gels 40
Figure 20: Sensor expansion ratio in matrices of varying stiffness 41
Figure 21: Stress-expansion ratio calibration curve 41
Figure 22: Viscoelasticity in live and fixed T47D spheroids 42
Figure 23: Dissipation of viscoelastic properties in invasive spheroids 43
Figure 24: Local viscoelastic changes in inducible invasive MCF7-Src spheroids 44

List of Tables

Table 1 – pNiPAAm Hydrogel Formulation 27
Table 2: Formulations of polyacrylamide phantom gels 30

List of Abbreviations

2D – Two Dimensional

3D – Three Dimensional

AFM – Atomic Force Micriscopy

DMEM – Dulbecco's Modified Eagle Medium

ECM – Extracellular Matrix

MRE – Magnetic Resonancce Elastography

OCE – Optical Coherence Elastography

pAAm – Polyacrylamide

PBS – Phosphate Buffered Saline

pNiPAAm – poly-n-isopropylacrylamide

TEMED - tetramethylethylenediamine

TFM – Traction force Microscopy

1. Introduction

1.1 Motivation

The mechanical properties of tissues, especially stiffness, is an established indicator for the presence of some diseases, such as with many soft tissue cancers, which has made it an essential characteristic used in screening[1–3]. While very effective in this context, there remains the challenge of understanding what is happening within a tumor *in vivo* which could be indicative of disease progression[3]. By developing techniques to measure the mechanical properties of tissue, new information about the diseased tissue can be acquired and potentially used to inform more appropriate treatment options, improving patient outcomes. The importance of tissue mechanical properties however is not limited to cancer and has been shown to be an important factor in other diseases, tissue development, homeostasis, and general cell behavior[3,4]. With such widespread impact across biological systems, it is imperative to develop techniques engineered to function at the scale of a cell to allow understanding of the local environment in tissues as experienced by cells.

As evidenced in the numerous studies of tumor stiffening, tissue mechanics are dynamic and highly heterogenous which means individual mechanical property measurements are only a snapshot in time and space of the tissue[2,5,6]. They therefore may not be indicative of how the tissue is changing or how those properties vary across a tissue. In 3D cultures used to better emulate tissues *in vivo*, the cells themselves both determine and change their local environment mechanically so it is especially important to characterize what a cell would mechanically sense as they are often distinct from the bulk tissue properties[7,8].

While cells have been shown to respond to surrounding matrix stiffness, the viscous properties of a matrix have emerged to be potentially as influential on cell behavior both on a 2D substrate and in a 3D matrix[9,10]. These findings suggest that cells can discern time dynamics independent of stiffness when probing their local environment which makes the widespread use of linearly elastic substrates for tissue culture potentially limiting to studies in mechanobiology. With both matrix stiffness and viscous properties being distinguishable by cells, there may be interplay between the properties which drives cell form and function[11]. Therefore, both the stiffness and viscous time dynamics of a tissue could be used in combination to better characterize why cells behave the way they do and why they may be driven to change in response to their environment. Given that tissues are well regarded as being viscoelastic, it is evident that cell-scale viscoelasticity could inform our understanding of what a cell feels within a tissue while remaining in the confines of a tissue as opposed to a 3D culture substrate[12,13].

By modelling and evaluating cell-scale viscoelasticity in 3D tissues, we can begin to understand the implications of both the elastic and viscous properties of tissues on development, especially in the context of disease where changes to the tissue's stiffness are already evident.

1.2 Aims

The aim of this work was to adapt previously used thermally actuated mechanosensors for use as viscoelastic sensors which could be used to evaluate cell-scale viscoelasticity in relatively stiff tissues[14]. With no previous sensor being able to probe the viscoelastic properties within stiff tissues, this development permits future studies in mechanobiology to better understand how

time dependent viscous properties may contribute as essential mechanical factor sensed by cells. This is completed through the following three aims:

1) Characterize sensor stress-expansion profile through constrained expansion in linearly elastic matrices.
2) Develop an inverse finite element model to measure viscoelastic properties of tissues from experimentally obtained strain-time profiles.
3) Evaluate viscoelastic properties in breast cancer spheroids to investigate changes with invasive phenotypes.

2. Background

The mechanical properties of tissues have long been established as drivers of tissue form and function[4]. With differences in the stiffness of various types of tissues being so distinct, ranging from 10s of pascals in soft tissues and 100s of megapascals in bones, no single measurement technique can have the resolution and range needed to. precisely characterize all tissues[15]. In addition, it has been shown that small mechanical changes to the 2D and 3D substrates which cells are seeded on is influential on cell behavior[16–20]. With such extensive variability across different types of tissues along with cells being sensitive to small changes in their cellular microenvironment, it is evident that specialized techniques are needed to advance our understanding of tissue mechanics. However, probing a macro-scale tissue made up of meso-scale cells that respond to micro-scale elements of the cellular microenvironment is highly complex[3]. With interest in tissue viscoelasticity growing as evidenced by the frequency of publications increasing steadily with time shown in figure 1, it is essential that suitable techniques for evaluating viscoelasticity across the wide range of tissues becomes available.

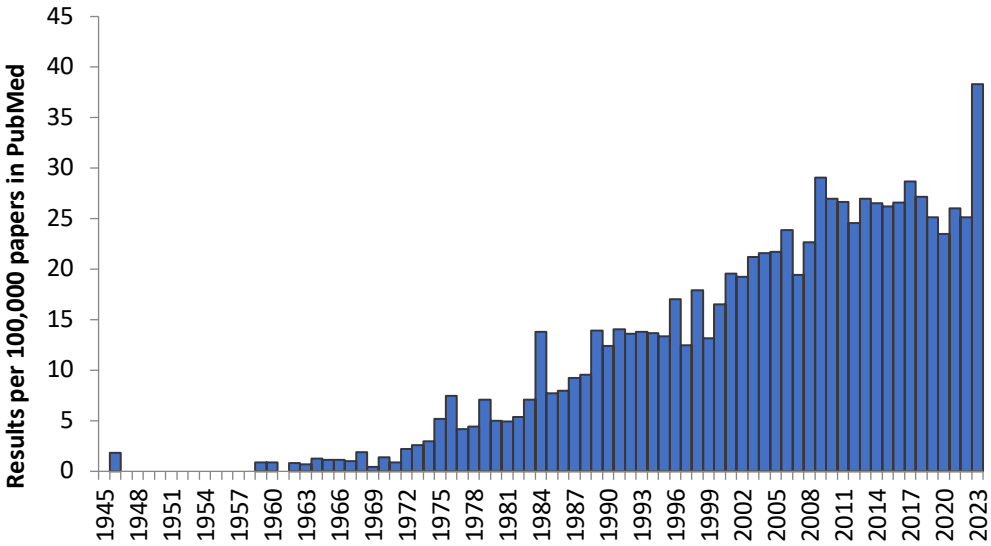

Figure 1: Publication in PubMed with the keyword 'Tissue Viscoelasticity' by year.

2.1 Basics of mechanical properties

In its most basic form, materials can be characterized as linearly elastic through the relationship of stress and strain, that is the force applied over an area and the normalized change in length of the material being stressed shown in figure 1 (a). Most simply the stress (σ) and strain (ε) of material are linearly related and characterized by the Young's Modulus (E) of the material which defines the stiffness of the material at levels of strain where no permanent deformation occurs shown in figure 2 (b). While loading of a material causes deformation in the same direction as the applied stress, there is also deformation that occurs perpendicular to the direction of the applied stress because of incompressibility in the material which is described by the Poisson ratio (ν) of the material. The Poisson ratio is calculated as the ratio of transverse strain to axial strain on a stressed material as described in figure 2 (c). As illustrated in figure 2 (d), when continually increasing applied stress, the yield point is eventually reached after which permanent plastic

deformations begin to occur and remain after applied stress is removed. As stress is further applied, the material eventually reaches a point of excessive deformation and fractures.

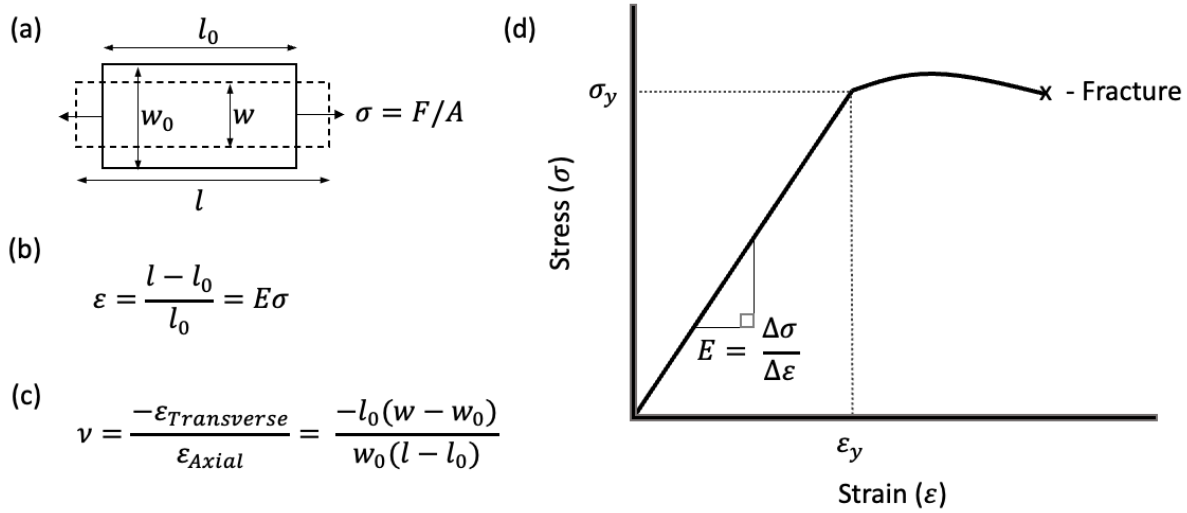

Figure 2: (a) Deformation of rectangular block from tensile stress at the ends results in longitudinal stretch of the material and corresponding lateral shrinking. (b) Definition of strain based on deformation with positive strain indicating tensile load and negative strain indicating compressive load. Strain is also equivalent to the product of stress and the Young's modulus over the elastic region of deformation. (c) Poisson ratio ν defines the relationship between deformation in the direction of and perpendicular to applied stress. (d) Representative stress strain curve for linearly elastic material up to its fracture point. Young's modulus (E) is denotes the slope over the linear range of stress and strain.

While stress can be applied normally to the surface, it can also be applied tangential to the surface in what is called shear stress illustrated in figure 3. In the same way as materials can deform elastically to a stress normal to the surface characterized by the Young's modulus, they can also be characterized by the shear modulus (G) which describes the linearly elastic relationship between shear stress (τ) and shear strain (γ).

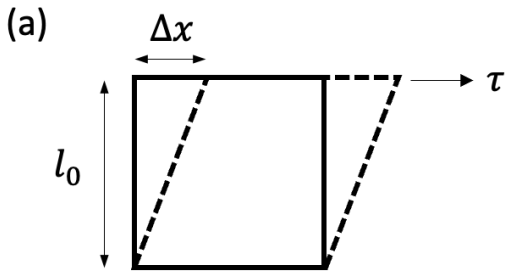

(b) $\tau = \frac{F_{Transverse}}{A}$

(c) $\gamma = \frac{\Delta x}{l_0}$

(d) $G = \frac{\tau}{\gamma}$

Figure 3: (a) Shear stress (τ) applied on a test cube causes alteral deformation of the sample. (b) The shear stress is defined as the average force tangential to the surface of area A. (c) Shear strain is defined in engineering terms as the ratio of lateral deformation (Δx) to the initial length of the surface. (d) The shear modulus (G) defines the ratio of shear stress to shear strain over the elastic range of deformations.

While Young's modulus and shear modulus are distinct, they can be related through the following equation which also includes the Poisson ratio (ν) defined in figure 3 (c).

$$E = 2G(1 + \nu)$$

2.2 Static vs dynamic moduli

Unfortunately, the Young's modulus and shear modulus characterize only the static properties of a material and do not account for how a material may respond dynamically to loads and deformations. Instead, oscillatory tests are performed over a range of deformations to obtain the dynamic moduli of a material. Dynamic tests are more suitable to characterize materials that are viscoelastic rather than exhibiting linear elastic behavior. Just as with static moduli there are separate dynamic moduli for normal and shear stresses which are still denoted by E and G. The difference is that dynamic mechanical testing evaluates both a storage and loss modulus which measure the ability for a material to store and dissipate energy when deformed, accounting for the viscous behaviors seen in many materials. With compression and tension, the storage and loss moduli are given as E' and E'' while the shear storage and shear loss moduli are denoted as

G’ and G’’. In linearly elastic materials, the loss modulus is negligible and therefor the storage modulus is equivalent to the Young’s or shear modulus respectively.

2.3 Challenges in measuring tissue mechanical properties

While changes to the mechanical properties external to tissues can be completed relatively easily by changing the matrix surrounding the tissue[16–20], internal changes which are driven by the tissue itself are much more difficult to evaluate and require the use of specially engineered techniques to make such measurements. Essentially, cells are responsive to their environment through signaling factors including mechanical probing which are made up by the tissue itself *in vivo*. While tuning matrix properties in 2D and 3D can elucidate the response to cells to their changing environment, it does not detail the dynamic changes that occur in larger scale tissues that change dynamically as they develop.

Furthermore, the information obtained by the measurement technique is specific for the length-scale, location, and time-scale of the measurement which limits comparison of techniques[3].

2.4 Techniques for tissue mechanical property measurement

Regardless, there is a multitude of different techniques that have been developed for the measurement of tissue mechanical properties. In general, these techniques require applying a stress or strain and measuring the corresponding other property. These techniques can be categorized by their length-scale and location of measurement as surface based, internal or bulk. These spatial distinctions substantially change what is measured with bulk measurements being indicative of the tissue scale mechanical properties while surface and internal measurements can

range from macro-scale (millimeter range) and cell-scale (micrometer range) mechanical properties.

2.4.1 Bulk measurement techniques

Most conventional are techniques which measure the bulk mechanical properties of tissues, in part due to the ease of making larger scale measurement and the extensive research into characterizing materials at a scale of millimeters to centimeters. Relative to tissues, this type of measurement characterizes average properties across the whole of the tissue without any spatial variation. This type of technique is most appropriate for a homogenous tissue sample however it has been shown that despite uniformity in the type of cells and overall makeup of a tissue, there can still be considerable variability in the mechanical properties at a higher resolution. Some techniques which have been applied to tissues are illustrated in figure 4.

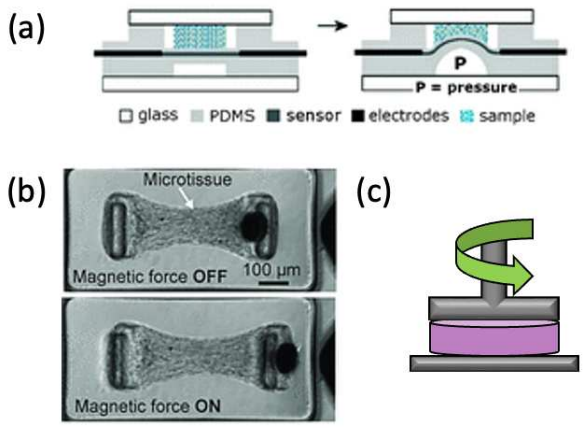

Figure 4: Bulk mechanical property measurement of tissues. Compressive measurements made through (a) microfluidic compression testers[21,22]. (b) Tensile measurements made through magnetically actuated pillars[24]. (c) Rheometer based mechanical property measurement based on shear stress and strain. (a) Reprinted with permission from MacQueen, L., Chebotarev, O., Simmons, C. A. & Sun, Y. Miniaturized platform with on-chip strain sensors for compression testing of arrayed materials. Lab. Chip 12, 4178–4184 (2012). (b) Reprinted with permission from Zhao, R., Boudou, T., Wang, W.-G., Chen, C. S. & Reich, D. H. Decoupling cell and matrix mechanics in engineered microtissues using magnetically actuated microcantilevers. Adv. Mater. Deerfield Beach Fla 25, 1699–1705 (2013).

Tensile and compression testing of materials are the most straightforward techniques whereby the sample is either pulled in tension or squished in compression. Samples are loaded axially with stress and strain being monitored during loading and the characterization of the stress strain profile yield the mechanical properties of the sample. These techniques have been adapted for use with tissue through miniaturized compression testers[23,25], microfluidic compression chambers[22], and pillar based magnetic microtissue testers[24,26] as illustrated in figure 4 (a), (b) and (c). These techniques are highly specialized to specific types of tissues and therefore cannot always be applied to specific tissue models or even excised tissues. Especially when considering tensile testing of a tissue, it is important to consider how that tissue can be connected to the testing apparatus.

Rather than axially loading samples, stress and strain can be applied tangential to the surface through shear rheology illustrated in figure 4 (d). To measure mechanical properties, shear stress is applied and shear strain in observed. Shear rheometers measure the shear modulus, G in static tests and the storage modulus, G' and loss modulus, G" in dynamic tests which characterize the stored energy from deformation and the lost energy dissipated through internal friction.

Lastly, stress can be applied through isotropic loading with osmotic pressure and mechanical properties can be inferred based on observed size change from compression[8]. By modulating the concentration of dextran, a long chain polymer unable to enter tissues, spheroids bulk mechanical properties have been assessed both as a linear elastic and viscoelastic material[27,28].

2.4.2 Surface measurement techniques

When measuring the mechanical properties over the surface of a tissue, there are many choices for techniques and flexibility in the length-scales which can be evaluated. Only direct contact measurement techniques are discussed and remote tweezer techniques were omitted as they operate at a sub-cellular scale and cannot probe stiff properties as applied forces are on the order of piconewtons and femtonewtons.

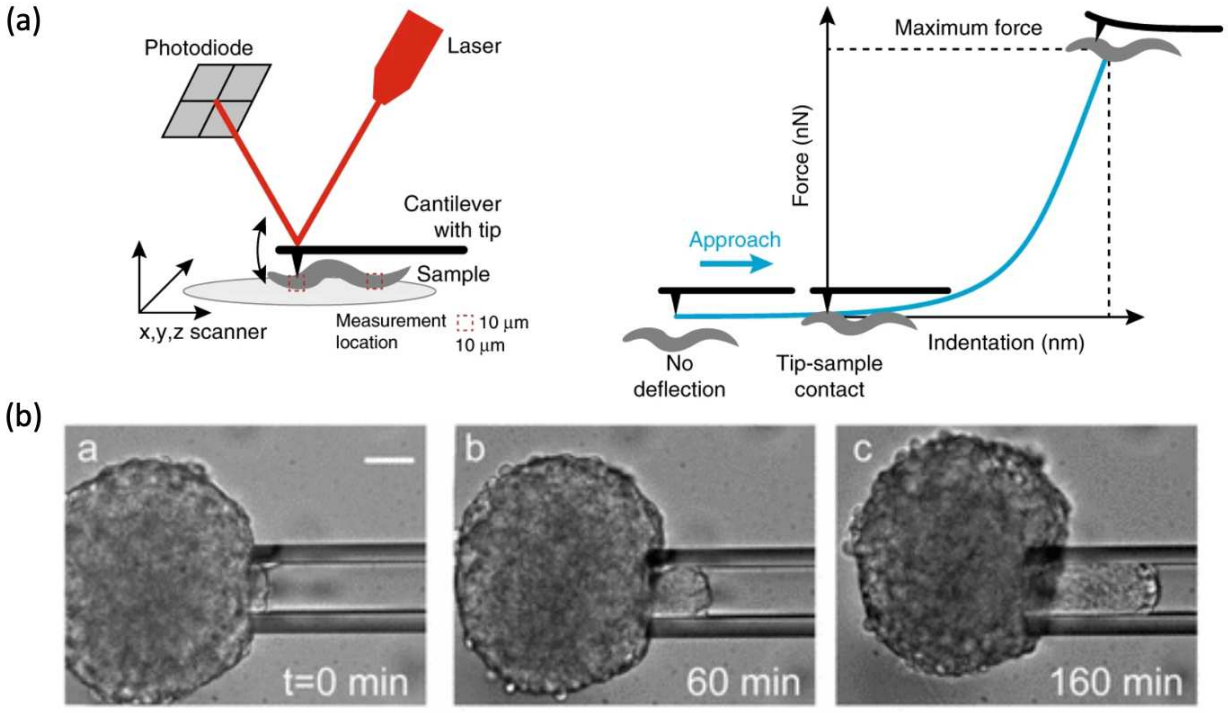

Figure 5: Surface mechanical property measurement of tissues. (a) AFM applies force onto the surface of a sample with cantilever tip deflection being indicative of both force and deformation allowing mechanical properties to be determined based on force indentation profile[29]. (b) Micropipette aspiration of spheroids to measure tissues viscosity from prolonged suction at spheroid boundary (Scale bar 50μm)[30]. (a) Reprinted with permission from Essmann, C. L. et al. Mechanical properties measured by atomic force microscopy define health biomarkers in ageing C. elegans. Nat. Commun. 11, 1043 (2020). (b) Reprinted with permission from Guevorkian, K., Colbert, M.-J., Durth, M., Dufour, S. & Brochard-Wyart, F. Aspiration of biological viscoelastic drops. Phys. Rev. Lett. 104, 218101 (2010).

Adapted from its original use in surface shape mapping, AFM (atomic force microscopy) has been used to characterize the mechanical properties across a surface with very high resolution[29,31,32]. The schematic of an AFM system and technique are summarized in figure 5 (a). Working on the

same principle of macro-scale compression tests, a small needle shaped probe is pressed into the surface to measure the stiffness of the sample. The resolution of the technique is as low as a few nanometers due to the precise design of the tip but can also be up to the scale of microns[33]. By probing across the surface of the tissue, a map of stiffness can be generated however this is mostly limited to flat tissue sections simply due to the geometry[29].

Analogous to AFM is micro and nano indentation where a probing head is again pressed into the surface and the resulting stress and strain are used to characterize the mechanical properties[34–36]. This technique is often used to characterize linearly elastic or viscoelastic materials and can be used over a range of length-scales by changing the size and shape of the indentation tip[37,38]. Depending on the size of sample, this technique can provide a lower resolution characterization of mechanical properties across a tissue section or be used to across the surface of a whole tissue sample. Furthermore, this technique while more coarse in its surface mapping can probe with substantially greater levels of deformation as AFM probing has a limited indentation depth and is more suited to capture individual cell mechanical properties than those of the outer layers of tissues[39].

The final direct contact method for measuring mechanical properties on the surface of a tissue is pipette and micropipette aspiration[30,40–42]. By applying a suction pressure on the surface of the tissue, the tissue is gently pulled into the tip of a pipette with the magnitude of deformation and the applied suction force being indicative of mechanical properties. Specifically, the bulge geometry is observed optically at the suction tip either at one timepoint or over time to elucidate the elastic or viscoelastic properties of the sample. The time course response of a tissue exposed to a suction force from micropipette aspiration is illustrated in figure 5 (b) illustrating the slow

viscous flow observable in tissues after hours of applied suction. This technique functions over a range of length-scales depending on the pipette tip geometry to measure properties of individual cells or larger tissue constructs. Micropipette and pipette aspiration have also been implemented in microfluidic chips through specially designed channels which perform the same suction function[43].

2.4.3 Internal measurement techniques

While bulk and surface techniques provide unique insight into tissue mechanics, the mechanical properties internal to a tissue are most indicative of what the average cell experiences, simply because most cells are internal to a tissue or organ. In addition, the properties of a tissue are unlikely to be the same at the surface compared to within for a multitude of reasons. Chemical factors must diffuse into a 3D tissue or be delivered through mass transport like in the circulatory or gastrointestinal systems. Furthermore, any kind of contact based mechanical transduction involves the outer surface experiencing different stresses than inside the tissue. Finally, cells near to the surface don't have the same 3D contact with cells in all directions and therefor experience a heterogenous mechanical environment more so than cells within the tissue. With cells cultured in 2D and 3D showing morphological differences, it follows that even in a 3D tissue we would see morphological(and potentially also mechanical) differences at the surface or internally[44,45]. For these reasons, it is unlikely that in complex 3D tissues the mechanical properties of tissues will be equivalent at the surface and internally.

In a clinical setting, elastography has been used extensively to evaluate tissue stiffness and viscoelasticity through magnetic resonance elastography (MRE) and ultrasound elastography[46–48]. Elastography techniques use distortions in the tissues which are subsequently observed and

used to infer mechanical properties. These distortions can be generated with physical pressing on the tissue surface, through sound waves in ultrasound or even from the pulse of a subject. In addition, the velocity of shear waves in the materials can also be translated to measure mechanical properties. These techniques function over a range of length-scales depending on the apparatus that is used. MRE has a resolution as low as half the resolution of native magnetic resonance imaging and ranges from 50μm to 10mm but is typically about 1-2mm[46,49–51]. Conversely, ultrasound elastography has a resolution that spans from 10μm to 1mm depending on the frequency of transducer used with high frequency leading to finer resolution. In optical coherence elastography (OCE), optical interferometry is leveraged to observe induced microstrains where resolution as low as a few micrometers can be obtained but imaging is limited in probing depth by light penetration limits[5,52–55].

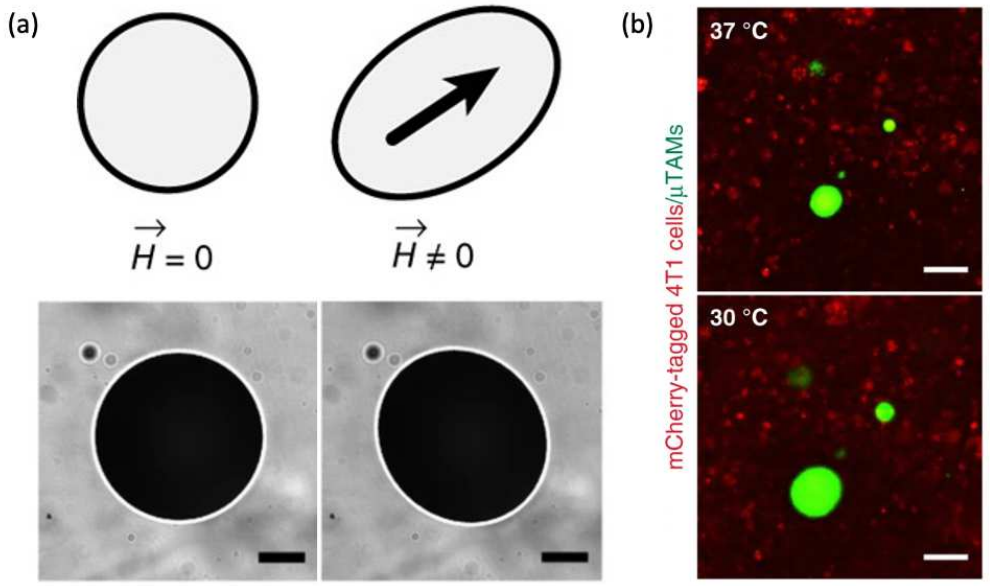

Figure 6: Internal mechanical property measurement techniques. (a) Magnetically actuated ferrofluidic oil droplets remain spherical until actuated by external magnetic field. Time dependent sensor deformation used to measure viscoelastic properties of surrounding matrix (Scale bar 100μm)[56]. (b) Thermally actuated expanding hydrogel sensors embedded in tissues resolve local elasticity from equilibrated sensor size change (Scale bar 50μm)[14]. (a) Reprinted with permission from Serwane, F. et al. In vivo quantification of spatially varying mechanical properties in developing tissues. Nat. Methods 14, 181–186 (2017). (b) Reprinted with permission from Mok, S. et al. Mapping cellular-scale internal mechanics in 3D tissues with thermally responsive hydrogel probes. Nat. Commun. 11, 4757 (2020).

Using ferrofluidic oil droplets, the viscoelastic properties of zebrafish embryos have been evaluate to investigate how mechanical properties change during embryonic development[56,57]. Under no magnetic field, the magnetic oil droplets take a uniform spherical shape but when a constant magnetic field is applied, the droplet begins to elongate parallel to the applied magnetic field. Based on the time dependent deformation of the tissue, the viscoelastic properties are deduced. This is illustrated in figure 6 (a) where the slight shape change of the oil droplet can be optically measured and computationally evaluated to determine viscoelastic properties of the tissues. Due to the small magnitude of sensor induced deformation, this technique is not suitable to thick tissues where light penetration challenges limit imaging accuracy and introduce significant error. Furthermore, the magnitude of stress applied by these sensors is very low and not suited to stiff tissues which would minimally deform when actuated.

In a similar sense, thermally actuated expanding hydrogel sensors formulated from the smart material poly-n-isopropylacrylamide (pNiPAAm) have been used to evaluate the local elasticity within breast cancer spheroids[14]. The hydrogel material is thermally responsive and become hydrophobic above 32°C which cause the polymer network to collapse and the sensors to shrink. When the temperature is brought below 32°C, the hydrogel becomes hydrophilic, and the sensor expands against the surrounding tissue. Based on the extent to which the expansion is constrained, the elasticity of the tissue is determined. An example pre and post sensor actuation images from sensors embedded in a tissue are shown in figure 6 (b) which illustrate how constrained sensor size change can be optically observed and the degree of sensor constraint permits inference of residual elasticity.

2.5 Viscoelastic modelling

Viscoelasticity describes both elastic and viscous properties of a material which can describe both the time dynamics of a material and the steady-state response once viscous effects have dissipated.

While simple as a concept, the modelling of viscoelastic materials faces the added complexity of varied constitutive models which each have unique responses to stress and strain. Most models consist of a combination of spring and dashpot elements to describe the linearly elastic and viscous properties of the sample. These elements can be added in series and in parallel with any number of independent elements in the model and each element describes a unique property of the material. While models can include many terms, simple constitutive models are often used as the physical implication of elements is easier to understand, estimation of parameters is less complex, and they are more generalizable across different systems. Examples of common constitutive models and the material responses to creep and stress relaxation are shown in figure 7. As evidenced by the varied creep and stress relaxation test responses, not all constitutive models are well suited for both tests due to limitations in how each elements behaves and contributes to the system in its entirety.

To test viscoelastic properties, usually either a creep test or stress relaxation test are employed. In a creep test, a constant step stress is applied to the material and the resulting deformation or strain is observed whereas in a stress relaxation test, a constant strain is applied to the material and the resulting stress is measured with time.

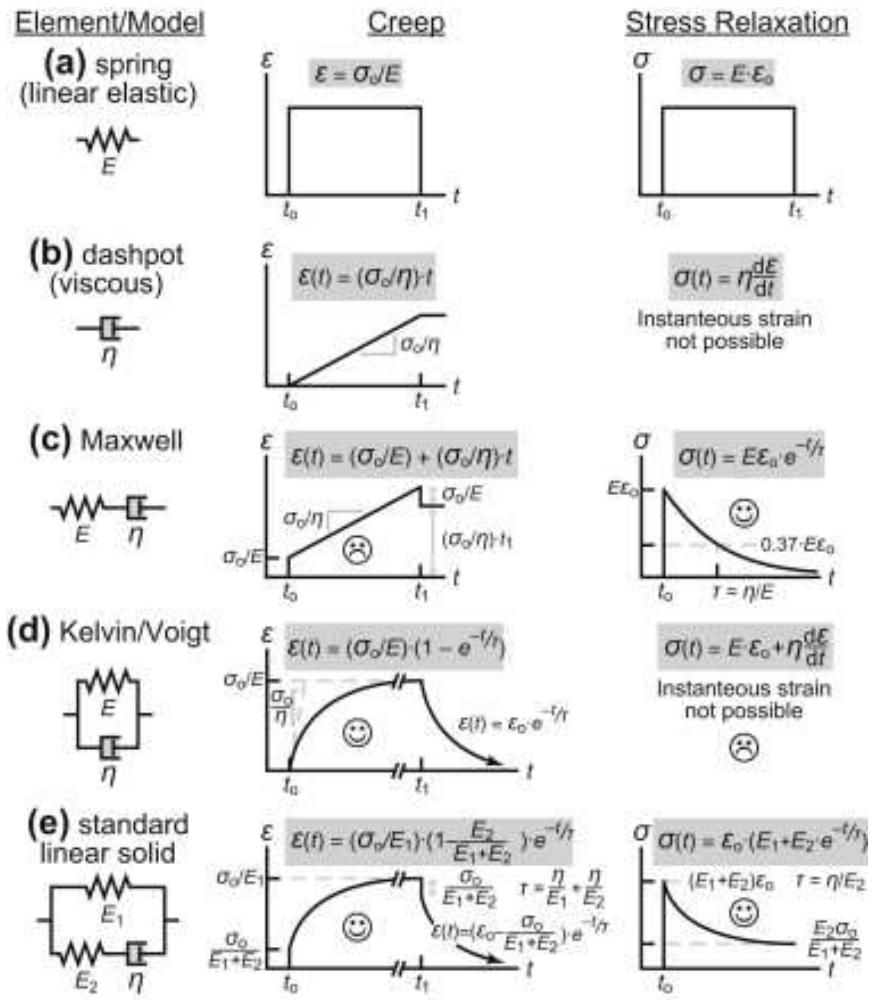

Figure 7: Common constitutive models for viscoelastic creep and stress relaxation, due to an instantaneous and constant applied stress (σ_o) or strain (ε_o)[58]. Response from tests on **(a)** a spring element, **(b)** a dashpot element, **(c)** the Maxwell model, **(d)** the Kelvin-Voigt model, and **(e)** the standard linear solid model. E is the elastic modulus of spring elements, η is the viscosity of dashpot elements, τ is the relaxation time, and t is time. Reprinted with permission from Roeder, R. K. Chapter 3 - Mechanical Characterization of Biomaterials. in Characterization of Biomaterials (eds. Bandyopadhyay, A. & Bose, S.) 49–104 (Academic Press, 2013). doi:10.1016/B978-0-12-415800-9.00003-6.

As evident by (a) and (b) from figure 7, single element models with a spring and dashpot are insufficient to resolve time dynamic properties of materials but by adding the two elements in series (c) or in parallel (d) allows either stress relaxation or creep properties to be evaluated. Unfortunately, these two model systems cannot exhibit both creep and stress relaxation due to how the elements contribute to the whole system. This limitation is solved by (e) the standard linear solid model for viscoelasticity which is a fusion of the Maxwell and Kelvin-Voigt models.

In the Maxwell model, a creep test cannot be performed as viscous strain occurs linearly and at a constant rate while the elastic component responds instantaneously. However, the Maxwell model can simulate stress relaxation as instantaneous strain placed on the system would first be absorbed by the elastic spring element and then dissipated by the viscous dashpot element over time.

Conversely, the Kelvin-Voigt model with a spring and dashpot element in parallel cannot exhibit instantaneous strain and therefor is not appropriate for stress relaxation tests. The Kelvin-Voigt model can however model creep behaviors of tissues where the dashpot element dictates the time dynamics of the creep, and the spring element dictates the steady state strain eventually reached by the system.

2.6 Mechanical properties as an indicator of breast cancer presence and progression

With many tumors, the disease is discovered through palpation whereby stiffening of the ECM (extracellular matrix) causes a noticeable lump to form[59]. Palpation however is only effective at estimating bulk tissue stiffness and further characterization of tumors is essential for evaluating the type of disease, monitoring disease progression and selecting treatment options[59].

In the preceding work to this, the residual stiffness of invasive and non-invasive breast cancer spheroids was evaluated and showed distinct differences in the variability of residual stiffness in the two conditions. While there was a relatively small difference in the mean or median residual stiffness, the invasive tissues showed greater variability with more locally stiff microregions being apparent.

Across the literature, there is shown to be significant variability in the reported elasticity of breast cancer tissues which in large part is due to the range of measurement techniques used and their corresponding length scale and spatial probing abilities. The lack of consistency in measurement techniques and lack of focus on the length scales of these measurements makes comparison between studies particularly challenging. However, characterization of mechanical properties across all length scales could be the key in understanding how processes at varying length scales contribute to eachother and potentially changes in one length scale could precede others and permit earlier detection of disease progression. It is therefore important to establish in general how these properties vary across length scales and how these properties may change independently from each other. While it is established that there is a stiffening in the bulk properties of a tumor, it is unclear how this stiffening develops from a microscopic to macroscopic change in the elasticity.

The Young's modulus of single cells from breast cancer cell lines has been evaluated which presents variability based on the techniques used. In differentially invasive MCF10A and MDA-MB-231 cells, the less invasive MCF10A cells exhibit generally wider ranging Young's modulus reading ranging from 200-1800 Pa as measured on the cells cytoplasm with higher stiffnesses resulting from greater indentation depths[60]. Conversely, the more invasive MDA-MB-231 cells exhibited lower Young's modulus values across indentation depths ranging from 200-300 Pa[60]. In another study evaluating stiffness of individual cells in MCF10A spheroids, micro-rheology was used and resulted in apparent Young's modulus readings ranging from 25-150Pa[61]. Evidently these ranges do not overlap which illustrates how the specific design of a system is an important factor to consider when evaluating mechanical properties. While both studies used the same

MCF10A cell line, the distinct change in internal cell stiffness is likely a result of the dynamic and responsive nature of cells which mechanically adapt under the vastly different environments of a 3D tissue and 2D substrate.

When looking at the slightly larger mesoscale, we once again get a very different picture of stiffness in breast cancer tissues. Through AFM mapping with a 5um probing head, diseased breast cancer sections showed average Young's modulus on the range of 400Pa for healthy tissue while diseased tissues had an elevated mean Young's modulus from this baseline due to small regions of very high stiffness exceeding 5kPa throughout the tumor[62]. In the preceding work to this, residual stiffness within 3D breast cancer spheroids were evaluated using thermally actuated hydrogel probes in both weakly invasive T47D cells and highly invasive. MDA-MB-231 cells. In this study, an increased heterogeneity was observed in the invasive MDA-MB-231 model resulting in residual elasticity readings ranging from 0.1-200kPa while the non-invasive T47D counterpart exhibited residual elasticities ranging from 0.4-10kPa[14]. While it is evident that there exists substantial heterogeneity at this length scale in breast cancer tumors between both studies, there is also substantially different elasticity readings between these two measurement modalities which suggests that again there are changes introduced on the tissue because of the requirements of the measurement technique. Especially in the case of probing sectioned tissues, the slicing of the tissue is sure to bring about mechanical changes within due to stress dissipation when cutting which makes the utility of non-disruptive probes like those used in the latter study more apparent as there is minimal change to native tissue architecture required to use the probes.

The bulk scale of tissue stiffness once again shows more variability between different morphologies of tissue samples. In the evaluation of breast cancer spheroids stiffness through microtweezer compression, there is substantial variability between cell lines used. In T47D spheroids, Young's moduli of 420Pa were found while MCF10A spheroids exhibited substantially greater stiffness at 1250Pa[63]. While within the range of values observed with mesoscale measurements, these moduli are low within this range and fail to capture the heterogeneity observed. At the same time, evaluation of *in vivo* breast cancer tumors through shear wave elastography (SWE) showed significantly higher stiffnesses in these tumors with mean stiffnesses ranging from 80-155kPa depending on the grade of tumor being evaluated[64]. Once again, there is a clear mismatch between different measurement techniques which, while evaluating very different systems of similar tissues, obtain vastly different values of the same property. This is particularly confusing as the mesoscale measurement of spheroids found local regions of very high stiffness which were comparable in magnitude to those found through SWE in primary tumors yet the microtweezers compression testing of spheroids saw much softer bulk stiffnesses even in the same cell lines.

2.7 Future Direction of the Field

While matrix stiffness is established as an essential mechanical property that determines tissue fate and function, tissue mechanical plasticity may provide further insight into the ease in which a tissue can reorganize which is potentially just as influential on fate and function[1,65]. Tissues often undergo transition from a jammed state, where cellular rearrangement is dampened, to an unjammed state where collective and individual cellular migrations are enhanced[66–71]. Cell jamming has also been linked to tissue development, tumor growth, cancer invasiveness and

wound healing, however, there are limited techniques to understand cell jamming's influence on these processes. Ultimately mechanical property measurements at a cell scale would provide the basis for understanding how cell jamming transitions are felt within 3D tissues by cells.

3. Approach

This work looks to extend the applicability of previously described stiffness sensors developed in the Moraes Lab at McGill University. Using the thermoresponsive properties of poly-n-isopropylacrylamide (pNiPAAm), spherical sensors could be actuated to expand within complex 3D tissues and sensor size change could be tracked through fluorescent microscopy. Based on the equilibrated size change of sensors after expansion in a constraining matrix, the local residual stiffness can be determined as illustrated in figure 8. This was first applied in spheroids made through a conventional aqueous two-phase system (ATPS) and through confinement in hydrogel micropockets. In these systems, a significant reduction in mean residual stiffness was seen in hydrogel micropocket confinement at 4kPa while spheroids formed with ATPS exhibited mean residual stiffness of 8kPa as evident in figure 8 (b). In spheroids made of non-invasive T47D cells and highly invasive MDA-MB-231 cells an increased heterogeneity of elasticity in the more invasive phenotype was found as illustrated in figure 8 (c). Finally, tumor progression towards metastases was evaluated in mice injected with T41 breast cancer cells in their mammary fat pads. As illustrated in figure 8 (d), an increasing number of highly stiff regions are found as tumors were given more time to develop and progress towards metastases.

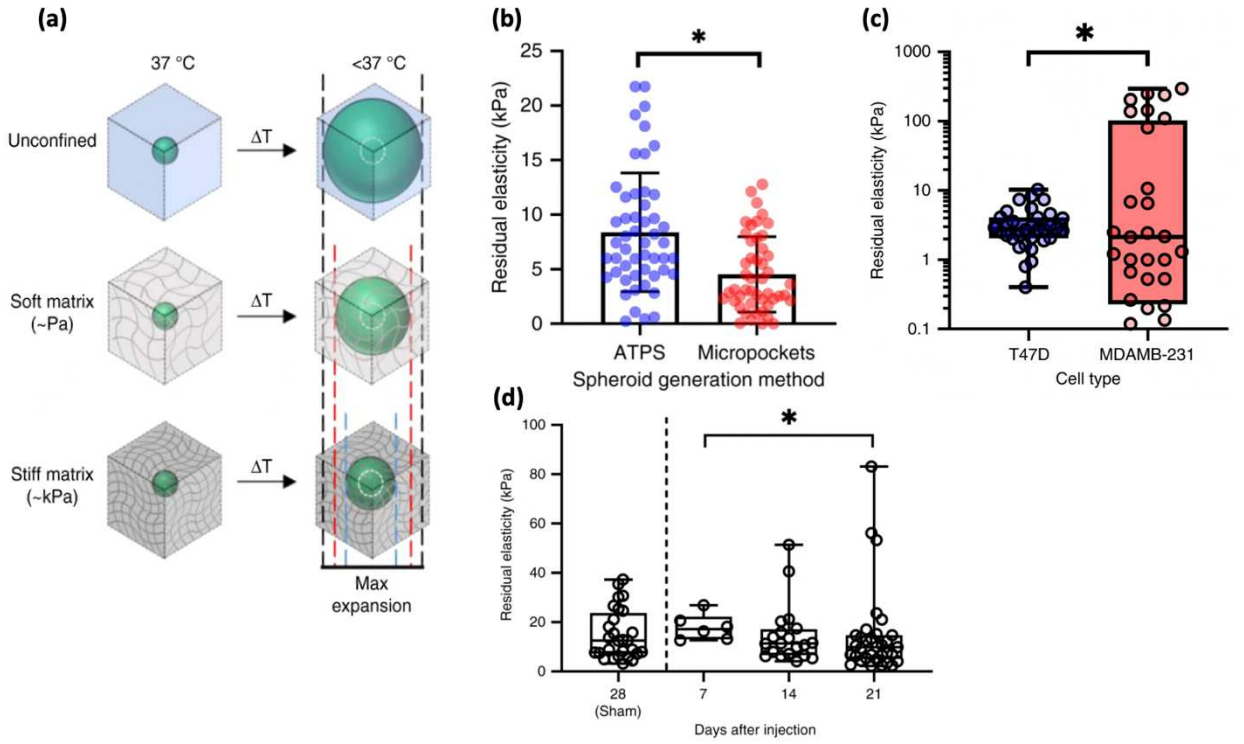

Figure 8: pNiPAAm sensors initial use in residual stiffness measurement. (a) Constrained expansion of pNiPAAm beads in differentially stiff matrices causes variable levels of sensor expansion permitting mechanical property inference. (b)HS5 spheroids generated through ATPS and micropocket spheroid aggregation techniques show significantly lower residual elasticities by hydrogel micrpocket confinement. (c) In differentially invasive T47D and MDA-MB-231 spheroids, there is a significant difference in residual elasticities with greater heterogeneity seen in the more invasive MDA-MB-231 spheroids. (d) Excised tumors from mice injected with T41 breast cancer cells show increased number of high stiffness regions as the cancer progresses towards metastases. Reprinted with permission from Mok, S. et al. Mapping cellular-scale internal mechanics in 3D tissues with thermally responsive hydrogel probes. Nat. Commun. 11, 4757 (2020).

While these sensors were very successful in evaluating residual elasticity within tissues at high throughputs, we wanted to adapt the sensors for viscoelastic measurement because the cellular microenvironment is not linearly elastic, and it is increasingly evident that viscous properties may be just as influential in mechanobiology as stiffness. Inspired by other works, particularly Serwane et al's magnetic oil droplets used in measuring viscoelasticity of developing zebrafish embryos, we wanted to see if our sensors could resolve creep behaviors in tissues if sensor actuation was adequately controlled. In theory, our sensors act like a spring which remain compressed until actuated at which point it expands at a rate and to a final size dependent of the viscous and elastic characteristics of the constraining matrix.

To adapt these sensors, we first had to resolve whether the time scale of sensor expansion was sufficiently fast to resolve differences in the viscous properties of tissues. While previous characterization had looked at the expansion ratio of sensors based on the elasticity of their matrices, we would need to extend this analysis to evaluate how stress is generated by sensors when confined and how that stress may vary for sensors of different sizes. Once characterized, we then developed an inverse finite element model to simulate sensor expansion which could be used to quantify the mechanical properties of tissues based on the expansion profile of sensors embedded within.

With well characterized sensors and a model to quantify sensors readouts, we could then apply the sensors to breast cancer spheroids as a first foray into resolving internal viscoelastic properties at a cell-scale in stiff tissues which had never before been done.

4. Materials and Methods

Unless otherwise stated, all chemical reagents were acquired from Sigma Aldrich (Oakville, ON) and cell culture materials from Fisher Scientific (Ottawa, ON).

4.1 Sensor fabrication

Sensors were fabricated using previously described methods with minor modifications to the protocol[14,72]. The basis of the sensors is a pNiPAAm hydrogel which has been doped with fluorescent polystyrene beads traditionally used in traction force microscopy (TFM) which improve bead edge clarity for image analysis. A general schematic of the fabrication process is shown in figure 9.

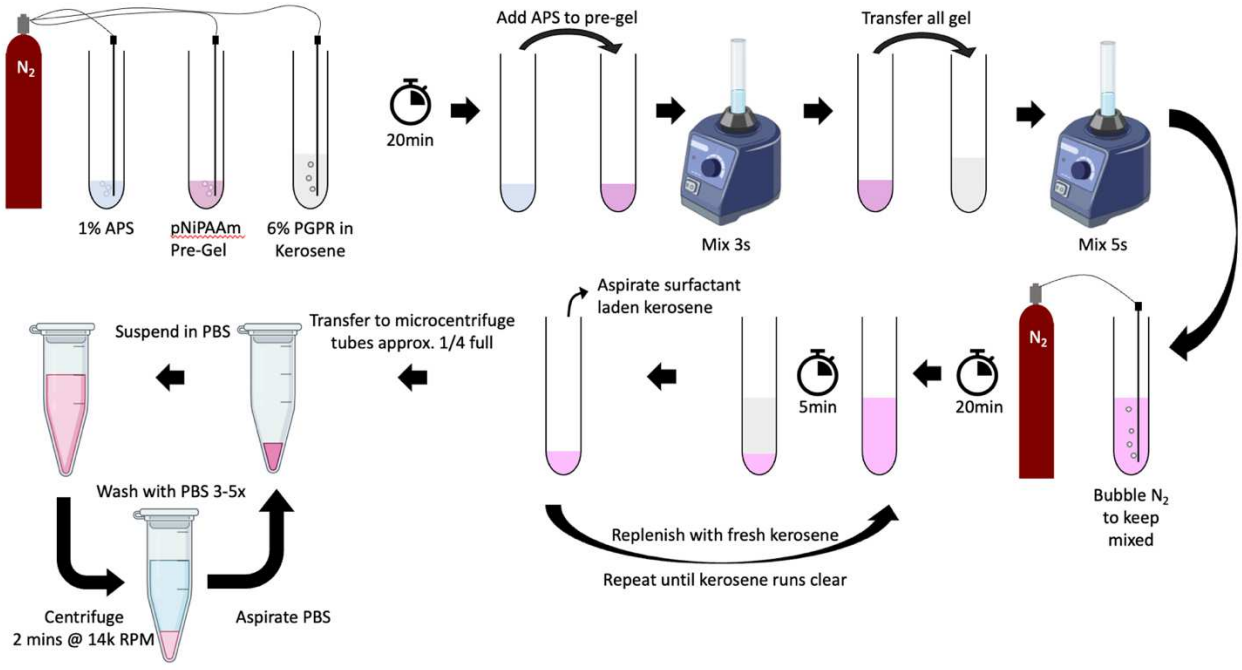

Figure 9: Schematic of pNiPAAm sensor fabrication. First pre-gel, initiator and oil phase are purged with nitrogen for 20 minutes. APS is transferred into the pre-gel and mixed to homogenized before being quickly transferred into the kerosene and vortexed to emulsify. Gels are left gently mixing under nitrogen bubbling to polymerize. To remove surfactant which crashes out of solution during PBS washes, multiple kerosene washes are performed until the kerosene top phase runs clear after sensors have settled. Sensors are subsequently washed with fresh PBS to remove all kerosene and surfactant.

A pre-gel solution of 20% (w/v) n-isopropylacrylamide (NiPAAm), 2% Bisacrylamide (Bio-Rad), phosphate buffered saline (PBS), tetramethylethylenediamine (TEMED), fluorescein-o-methacrylate in dimethyl sulfoxide (DMSO), and 0.2µm ⌀ red fluorescent polystyrene beads (Life Technologies) was prepared in a test tube according to

Table 1. A separate test tube of 1% (w/v) ammonium persulfate (APS) in PBS was prepared along with a third test tube of 6% (w/v) polyglycerol polyrincinoleate surfactant (PGPR 4150; Palsgaard, 90415001) in kerosene. Importantly, the volume of kerosene was at least double that of the pre-gel solution to ensure the liquid phase formed an emulsion in the oil phase.

Table 1 – pNiPAAm Hydrogel Formulation

NiPAAM (%)	**3**
Bisacrylamide (%)	**0.2**
20% (w/v) NiPAAm in PBS (µL)	150
2% Bisacrylmide (µL)	100
PBS (µL)	647.5
TEMED (µL)	1.5
100 mg/mL Fluorescein-o-methacrylate in DMSO (µL)	1
0.2µm ⌀ TFM Beads (µL)	5
1% (w/v) APS in PBS (µL)	100

With APS being sensitive to oxygen, the three test tubes were fitted with rubber septum stoppers, long 25G non-coring needles and shorter venting needles. Nitrogen was then bubbled through the 3 solutions for at least 20 minutes.

Once purged of oxygen, the required amount of APS (generally 100µL per 900µL of pre-gel mix) was drawn into a syringe and transferred into the pre-gel solution. The mixture was quickly

vortexed to homogenize before again being drawn into a syringe and added to the test tube of kerosene. Once added, the mixture was vortexed for a further 5 seconds to emulsify the liquid phase and generate spherical beads as illustrated in figure 10. The mixture was continually bubbled with nitrogen to gently mix the emulsion and avoid separation of phases.

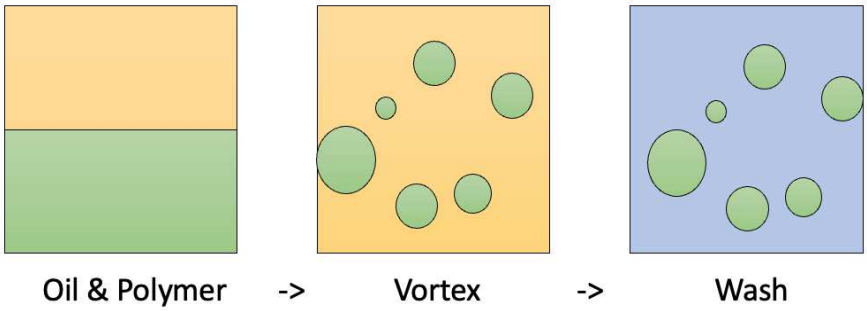

Figure 10: Sensor Oil-Water emulsion technique

After approximately 20 minutes, the pNiPAAm had gelled, and the beads were left to settle. Once the beads had settled to the bottom of the kerosene, the top layer of kerosene was removed, and fresh kerosene was added to wash away the surfactant from the surface of the beads. These kerosene washes were repeated until the top layer of kerosene started to become translucent, indicating the surfactant had been mostly removed. Insufficient removal of surfactant results in the remaining surfactant crashing out of solution when rinsing in PBS which is difficult to separate from the beads.

Once adequately free of surfactant, the top layer of kerosene was once again removed, and the bead solution was transferred to multiple Eppendorf tubes so that a further 1mL of PBS could be added to the tube. The Eppendorf tubes were then centrifuged at 14,800 $\times$ g for 2 minutes and the supernatant was aspirated. This was repeated 3 times before transferring the bead

suspension to a new Eppendorf and repeating once more. The beads were then stored in PBS at 4°C overnight to allow for full expansion.

To make sensors suitable for tissue culture, beads were coated with collagen I to allow attachment with cells and integration into tissues. Coating was completed using hetero bifunctional crosslinker sulfo-SANPAH as commonly performed with acrylamide gels[14,18,73–77]. To do so, sensors were first sterilised under UV for about 1 hour before being centrifuged. From this point, all work was done in a biological safety cabinet (BSC) with sterile reagents. Sensors were washed once more with sterile PBS, centrifuged, and then resuspended in a 0.1mg/mL sulfosuccinimidyl 6-(4'-azido-2'-nitrophenylamino) hexanoate (sulfoSANPAH) in sterile PBS and left under UV for 4 minutes. The sensors were once again centrifuged and treated once more with fresh sulfoSANPAH solution for another 4 minutes under UV. After a final centrifugation, the sensors were resuspended in a solution of 0.1 mg/mL collagen I solution in PBS and left overnight at 4°C to incubate. The following day, sensors were centrifuged and resuspended in sterile PBS.

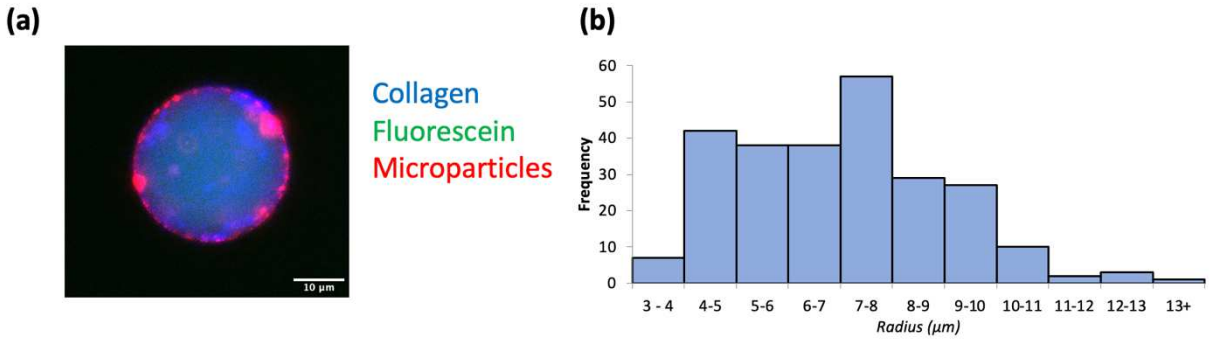

Figure 11: Stain of collagen coating and compacted sensor size distribution. (a) Collagen I staining of sensors confirm successful coating of sensors. (b) Polydispersity of sensor size induced by the emulsion-based fabrication yields a compacted sensor size mostly within the range of 5-10um in radius.

4.2 Polyacrylamide phantoms and rheology

To establish what levels of stress were generated by sensors at every level of sensor expansion, sensors were cast in polyacrylamide phantom gels with formulations tuned to give a wide range of stiffnesses. Formulations of polyacrylamide were sourced from literature and modified to include 5 μL of bead suspension to provide sufficient sensors for multiple data points without overloading gels and potentially changing their bulk mechanical characteristics by creating nodes of differing properties throughout. The pre-gel mixture and APS initiator were both preheated to 40°C for sufficient time for sensors to fully compact. Gelation was also completed on a slide warmer set to 40°C to ensure sensors remained compact while gelation occurred. The phantom gels were washed in prewarmed PBS to rinse away and unreacted reagents before being imaged.

Table 2: Formulations of polyacrylamide phantom gels used to characterize sensor generate stresses. Formulations adapted from Tse et al., 2010[74] and Ma et al. 2020[78]. Young's modulus characterized through conversion of storage modulus measured through shear rheology.

Young's Modulus (Pa)	**55.8**	**507**	**1,170**	**7,580**	**18,600**	**106,000**	**167,000**
40% Acrylamide (μL)	187.5	187.5	187.5	187.5	300.0	300.0	400.0
2% Bisacrylamide (μL)	53.5	17.0	27.0	118.0	120.5	360.0	480.0
PBS (μL)	765	689	679	588	473	233.5	13.5
TEMED (μL)	1.5	1.5	1.5	1.5	1.5	1.5	1.5
Bead Suspension (μL)	5	5	5	5	5	5	5
1% APS (μL)	100	100	100	100	100	100	100
Total Volume (μL)	1000	1000	1000	1000	1000	1000	1000

Due to the elevated temperature of casting performed on the phantom gels, the mechanical properties of the gels differ from identical gels cast at room temperature. As a result, all phantom gels were characterised through shear rheology (Anton-Paar, MCR 302) after imaging sensor expansion with the measured stiffness values reported in table 2.

4.3 Tissue culture

The cell lines used include MDA-MB-231(ATCC: HTB-26), T47D(ATCC; HTB-133) and MCF7-Src(ATCC; HTB-22). The MCF7-Src cell line is an engineered line of MCF7 cells which have been transfected with an inducible gene responsible for increased invasiveness. The Src oncogene can be activated through the inclusion of the antibiotic doxycycline in culture media which had been engineered to be a promoter of the transfected Src gene. The genetically engineered cell line was provided by collaborators in the Luke McCaffrey Lab at McGill University, Montreal, QC.

All cells were cultured in DMEM (Dulbecco's Modified Eagle Medium) supplemented with 1%(v/v) Antibiotic-Antimycotic and 10%(v/v) FBS (Fetal Bovine Serum). Cells were grown in T25 and T75 tissue culture flasks until above 80% confluent at which point, they were detached with 0.25% Trypsin and resuspended at 16 million cells per mL in DMEM for use in spheroid fabrication. Cells were kept in an incubator at 37°C and at 5% CO_2 levels.

Tissues were fixed in 4% paraformaldehyde for 20 minutes at 37°C and subsequently rinsed with PBS for fixed tissue experiments. It is critical for the fixative to be prewarmed as sensors must remain in their compacted state throughout the fixation process to avoid sensor deformation being integrated into the tissue when fixed.

4.4 Micropocket spheroid formation

To generate uniform spheroids, a previously described PAAm micropocket system was implemented[79] and is illustrated in figure 12. In short, 3D printed negative molds of a disc containing an array of uniform spheres was used to cast pocket shaped cavities in the PAAm. To remove the device, an 18mm coverslip treated with 0.4%(v/v) 3-(trimethoxysilyl)propyl

methacrylate (MPS) in acetone was pressed onto the mold during gelation and the coverslip was lifted off the mould with the micropocket device attached after gelation. Devices were washed three times in PBS to rinse away any remaining unreacted pre-gel.

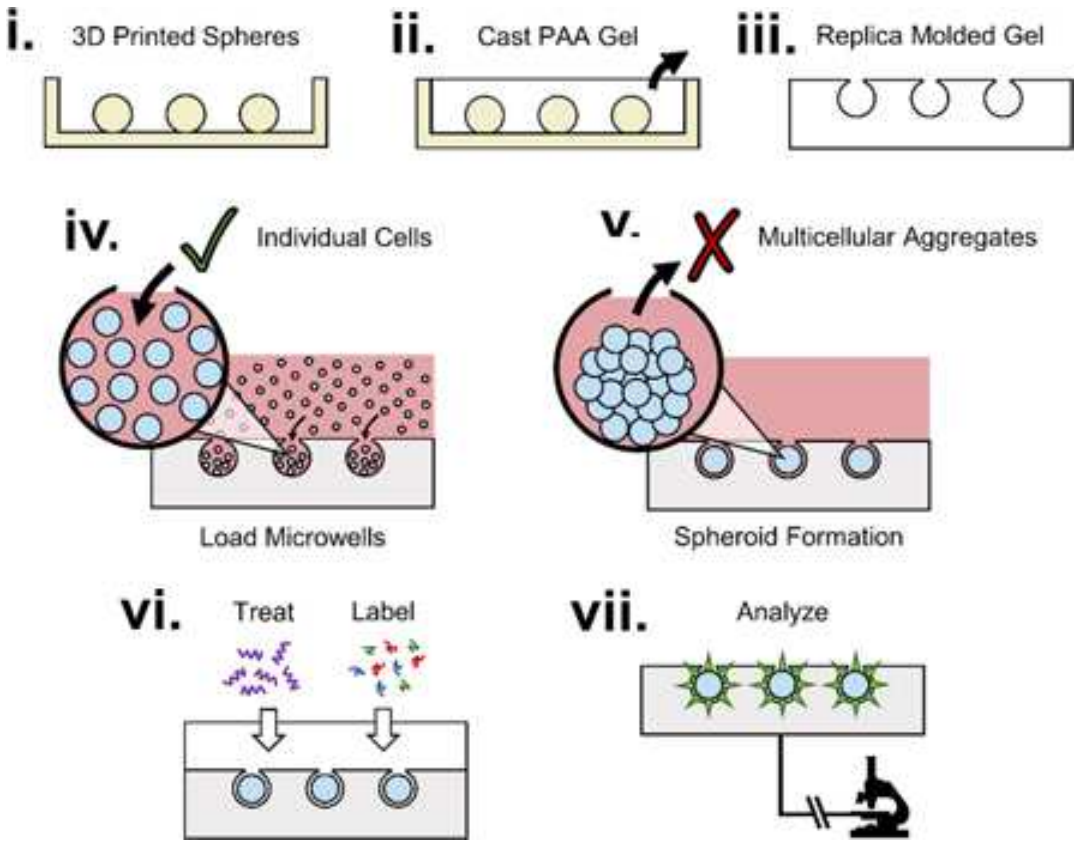

Figure 12: Micropocket device fabrication methodology[79]. 3D printed negative molds (i) are cast with polyacrylamide (ii) and after gelation are peeled out from the mold to give the replica molded micropocket gel (iii). Microwells can then be seeded with individuals dells iv) which can enter through the narrow opening but once they have aggregated into spheroids, the tissues cannot easily leave the pocket (v). The spheroids can then be used for further experimentation with the addition of treatment factors (vi) an also analyzed in site optically (vii). Reprinted with permission from Zhao, L., Mok, S. & Moraes, C. Micropocket hydrogel devices for all-in-one formation, assembly, and analysis of aggregate-based tissues. Biofabrication 11, 045013 (2019).

The coverslip with a micropocket device bonded was then adhered to the bottom of a six well plate with a drop of PDMS (Polydimethylsiloxane) and cured for approximately 4 hours at 40°C on a hot plate. PBS was added dropwise to devices to ensure the polyacrylamide gel did not dry out but also to not wet and dilute the PDMS during curing. Before use, micropocket devices were sterilized under UV for approximately 1 hour. Cells were suspended at 16 million cells/mL in

complete media and a further 5uL of bead suspension was added per mL of cell suspension. To seed the devices, 100uL of cell suspension was added onto the device, cells were allowed to settle for 5 minutes before the media was aspirated and a further 100uL was added. After another 5 minutes, the remaining media was again aspirated and 4mL of complete media was added to the wells, ensuring the devices were fully covered with media. Spheroids were left to form over 2 days in an incubator. Through the passive confinement, multiple sensors are embedded within each spheroid at random locations throughout the tissue.

4.5 Cold shock experiments

To actuate sensors, it was important to quickly drop the temperature past the transition point of pNiPAAm. To do so, PBS was frozen into small pieces which could be manually dropped into the well plates holding a sample. While not instantaneous, the small volume of media would still quickly drop below the transition temperature and sufficient ice was always added so that some solid ice was present over the course of an experiment. So long as the temperature of the sensor swiftly passed through the transition temperature of pNiPAAm, appropriate actuation would occur.

4.6 Finite element modelling

To simulate the expansion of sensors in matrices of both linearly elastic and viscoelastic properties, a 2D axisymmetric finite element model was developed in COMSOL Multiphysics v.5.3.1.201 (Comsol Inc., Burlington, MA, USA). As shown in figure 13, the geometry is made up of a large rectangle with a small hemisphere void at the center of the model. When revolved around the z-axis, we get a cylindrical geometry with a small spherical hole at the center. Rather

than model any dynamics of bead expansion, we simulated sensor expansion through the deformation induced in the surrounding matrix. As evident in the 3D revolution of the model, the geometry is made sufficiently large so that deformation or stress isn't transmitted to the boundary edge to adequately simulate a quasi-infinite matrix surrounding the sensor.

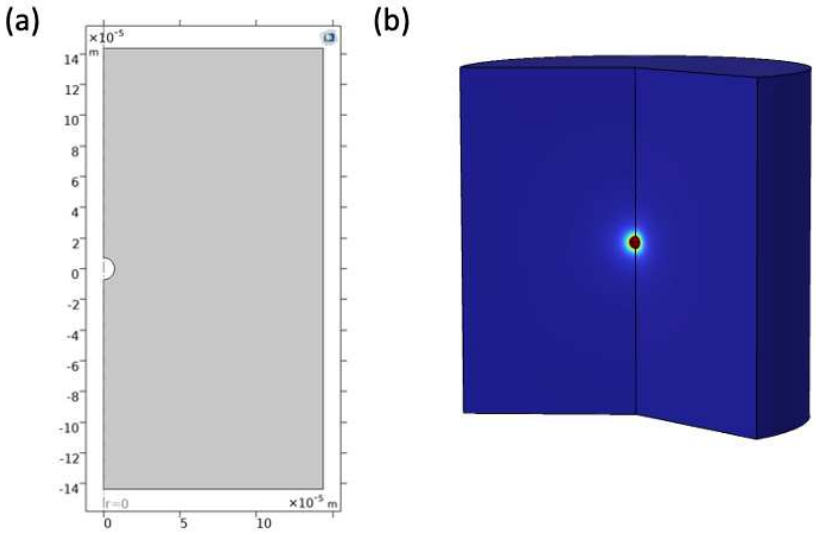

Figure 13: (a) 2D axisymmetric geometry used to simulate sensor expansion in linearly elastic and viscoelastic matrices. (b) 3D representation of model with model displacement colorized.

The boundary conditions selected for the model are illustrated in figure 14 (a). At the bead matrix interface, a boundary load applied with the stress sensor relation being described in the results section. A 2 second ramp function was implemented to improve convergence of the model as application of a high stress so abruptly could not be resolved. Along the z axis there is the axial symmetry condition due to the 2D axisymmetric geometry of the model. Finally, the outer boundaries were given a fixed boundary conditions to pin the model in place as during simulations, the geometry would float away if a free boundary condition were used.

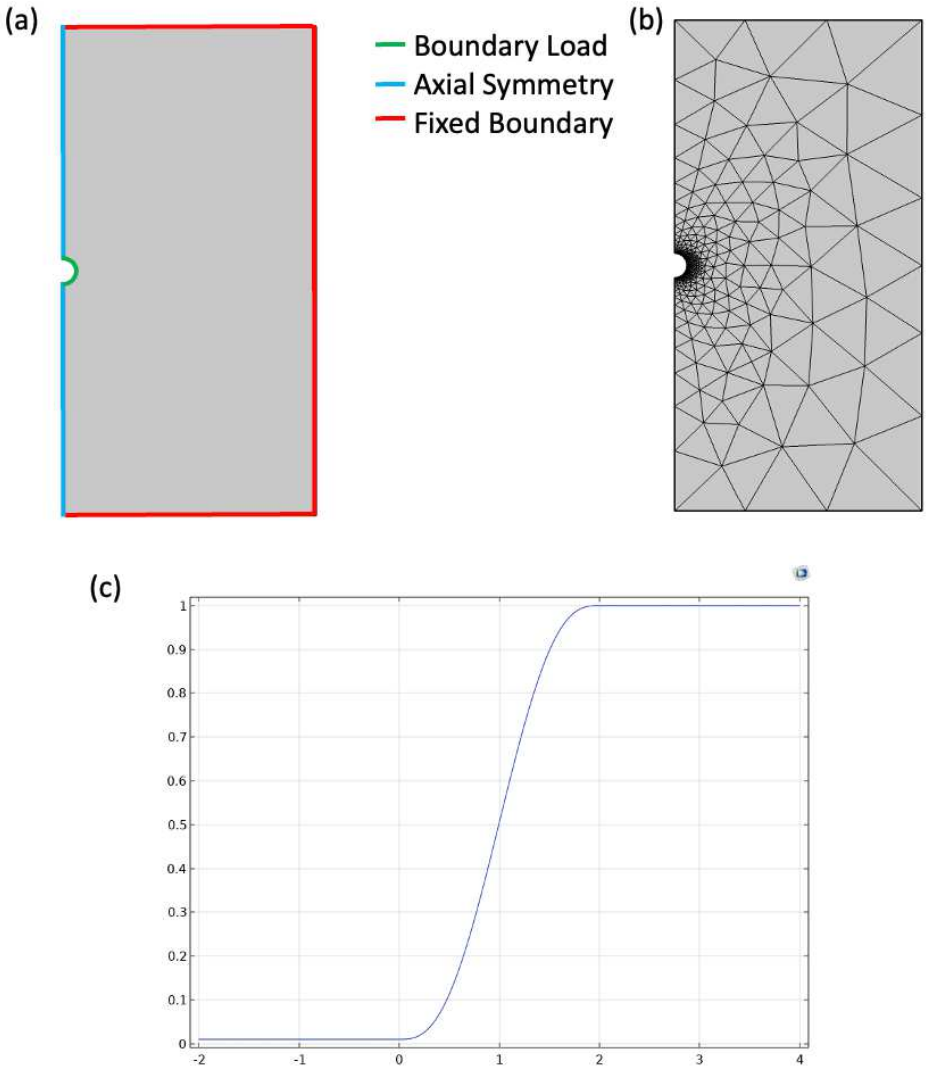

Figure 14: (a) Boundary conditions around 2D axisymmetric model used in simulations. (b) Free triangular meshing generated with reduced element size near region of bead expansion to resolve fine changes. (c) 2 second ramp function applied to boundary load condition to improve convergence.

The meshing of the geometry uses a free triangular mode with a 0.1 curvature factor to give smaller elements near the boundary load. This was important to resolve the high levels of deformations around the sensor. The meshing was optimized to give a coefficient of variation below 1% while also maintaining mesh element quality above 0.9. Only 1 domain is used in the model which represent the surrounding matrix around a bead. The domain was set as either a

linearly elastic matrix for stationary polyacrylamide phantom simulations or as a viscoelastic material with the Kelvin-Voigt model for time dependent simulations in spheroids.

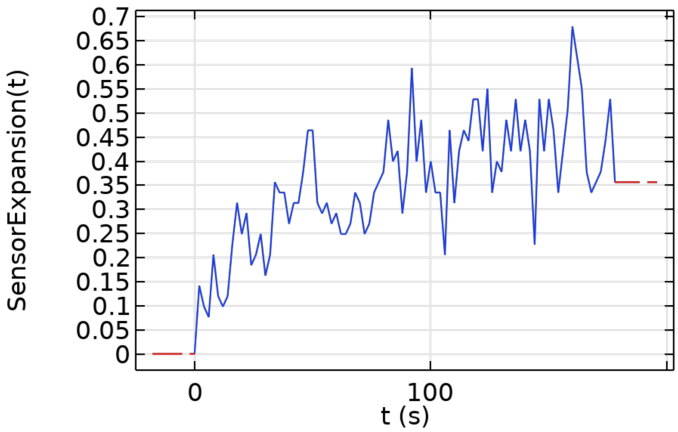

Figure 15: Sample experimental data processed by COMSOL interpolation function for input to optimization module.

Finally, the optimization module was implemented to fit the model sensor expansion profile to experimentally determined expansion profiles by modulating parameters of the Kelvin-Voigt model of viscoelasticity, Young's modulus E[Pa] and time constant τ[s]. The viscosity of the material can be obtained as the product of Young's modulus and the time constant. The SNOPT (Sparse Nonlinear OPTimizer) non-linear solved was selected with an optimality tolerance of 0.0001 to ensure a good fit. A sample experimental sensor expansion profile with the COMSOL interpolation function applied is illustrated above where individual data points are connected through a linear interpolation function which connects each point with a straight line. Variability in the experimental sensor expansion profile is due to the manual bead size measurements made when fitting circles around beads in ImageJ. All simulations were either 180 or 300 seconds long and should the experiment data not reach extend over the entire time course (due to sensor expansion not being only once the cooling has reached the tissue), the final expansion state was assumed constant over the remainder of the simulation.

5. Results

5.1 Bead expansion time dynamics

For sensors to be able to resolve creep behaviors, it was then critical to demonstrate that sensor actuation was swift, and the time dynamics of free expansion were sufficiently short to resolve longer creep behaviors when embedded in tissues. By embedding sensors in a very low stiffness collagen gel, we were able to resolve the minimum time for sensors to expand post actuation which was on the order of a few seconds. The sensor expansion profile is shown in figure 16.

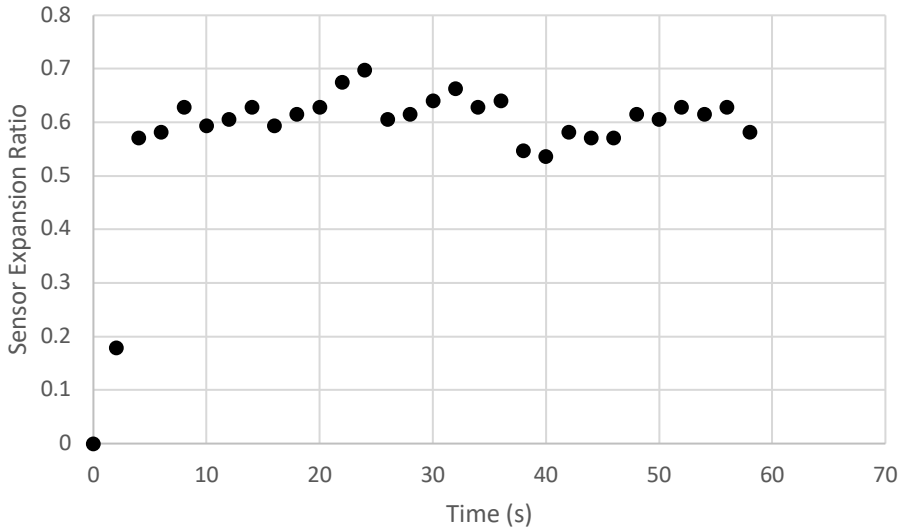

Figure 16: Sensor expansion in weakly constraining matrix demonstrates short time span of sensor actuation

As evident above, sensor expansion in a linearly elastic matrix is fast with full expansion occurring in about 6 seconds. While not instantaneous, this is sufficiently fast to resolve longer timescale viscous properties of matrices and we now have an indication of the smallest values of time constants which the sensors will be able to resolve.

5.2 Sensor calibration

To characterize the stresses generated by sensors during expansion, it was important to first understand how sensor size, matrix elasticity, and the displacement of the matrix relate to stress. To do so, the 2D axisymmetric model was given linearly elastic properties and the Young's modulus was swept along with the applied pressure at the boundary for multiple sensor sizes shown in figure 17. Pressure was selected as the boundary condition as opposed to force per unit area or total force as pressure always acts normal to the surface. The other boundary load conditions require describing the force in both the r and z directions of the geometry which likely would introduce unwanted shear stresses at the boundary due to numerical error.

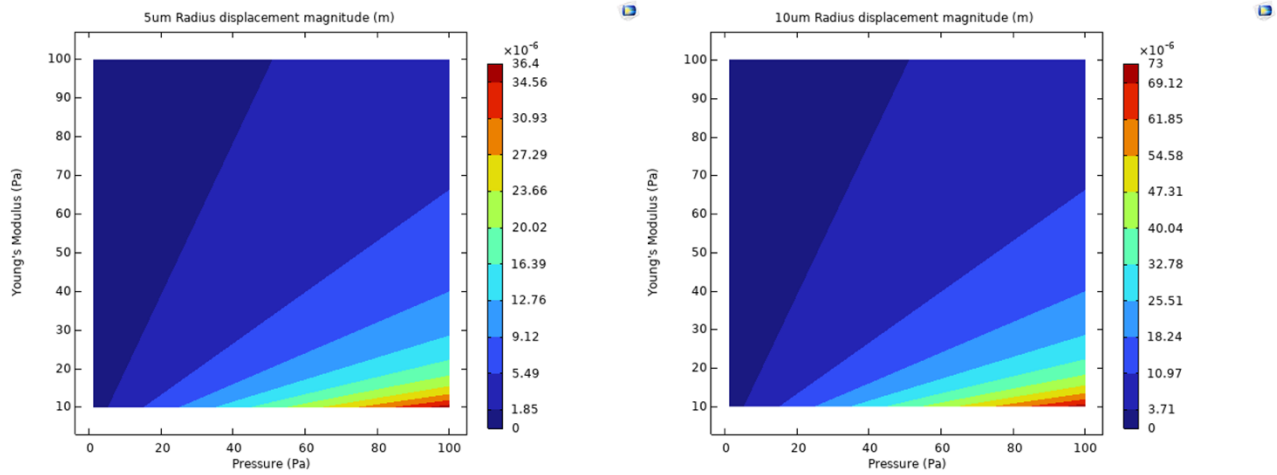

Figure 17: Verification of the relationship between sensor radius, applied sensor pressure, matrix Young's Modulus, and resulting matrix deformation.

Sensors of different sizes were evaluated in the linearly elastic material, and it was discovered that matrix displacement ($u = r_{expanded} - r_0$) could be related to sensor radius (r_0), matrix elasticity in the form of Young's modulus (E), and boundary pressure (p) by the following equation.

$$p = \frac{u \times E}{r_0 \times 0.72754} = \frac{R \times E}{0.72754}$$

With this relationship, it is evident that the expansion ratio ($R = u/r_0$) and the Young's modulus (E) were all that was needed to characterize sensor stress from expansion in linearly elastic matrices.

Sensors were then embedded in polyacrylamide phantom gels of varying stiffness as reported in Table 2. Three identical gels were cast for each formulation so that shear rheology could be performed after imaging to characterize the linear elastic properties of the gels. The rheology results are shown below.

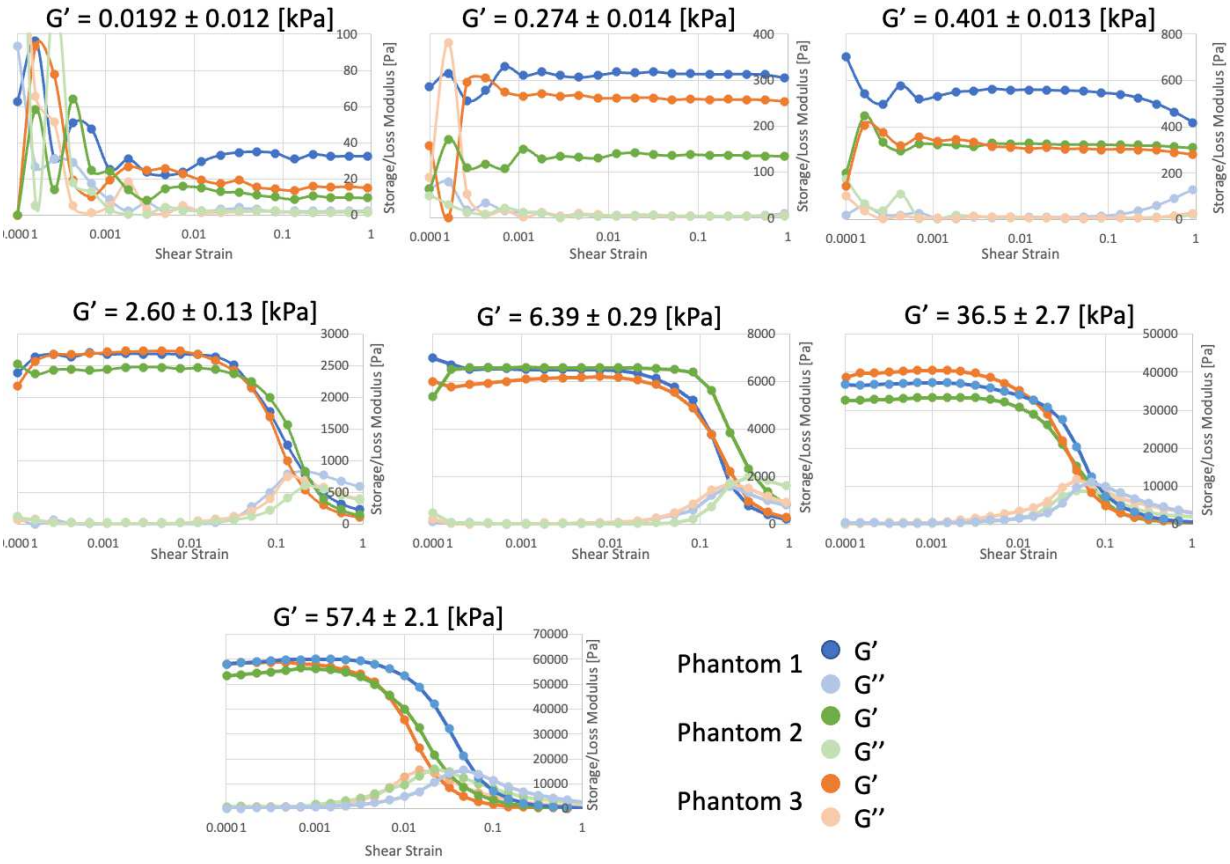

Figure 18: Shear Rheology of polyacrylamide phantoms illustrating linear elasticity over a range of applied strains. Storage modulus values were taken as the average over the plateaus of Storage modulus readings.

The storage modulus was converted to the Young's modulus with the assumption that the Poisson ratio of 0.457 for polyacrylamide found in literature was constant over all the formulations tested[80].

With polydispersity in the sensors already being evident, it was important to evaluate what influence bead size may have on the expansion ratio (R) of sensors embedded in matrices of equivalent stiffness. To do so, the deviation from the mean expansion ratio for sensors embedded in each stiffness of polyacrylamide was evaluated based on collapsed sensor size and is plotted in figure 19.

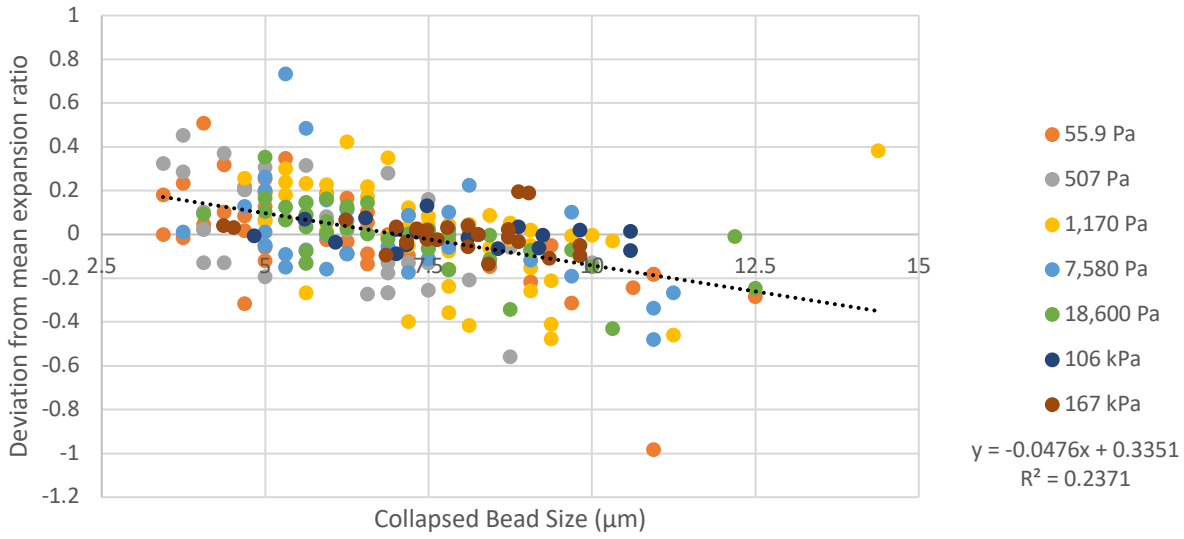

Figure 19: Deviation from mean expansion ratio for sensors in phantom gels of each stiffness (given as Young's Modulus E). Linear fit for all data points shows large sensors exhibit slightly lower expansion ratios in linearly elastic matrices but variability with size is relatively small.

It is apparent that sensor size does influence corresponding expansion however this size-based deviation is relatively small across the range of sensor sizes. To minimize error due to this variability, only sensors between 5 and 10 um in radius were used in viscoelasticity experiments.

With polyacrylamide phantom stiffness characterized, we could begin to piece together the sensor stress profile during expansion. First, we evaluated how sensor expansion related to the elasticity of the surrounding matrix.

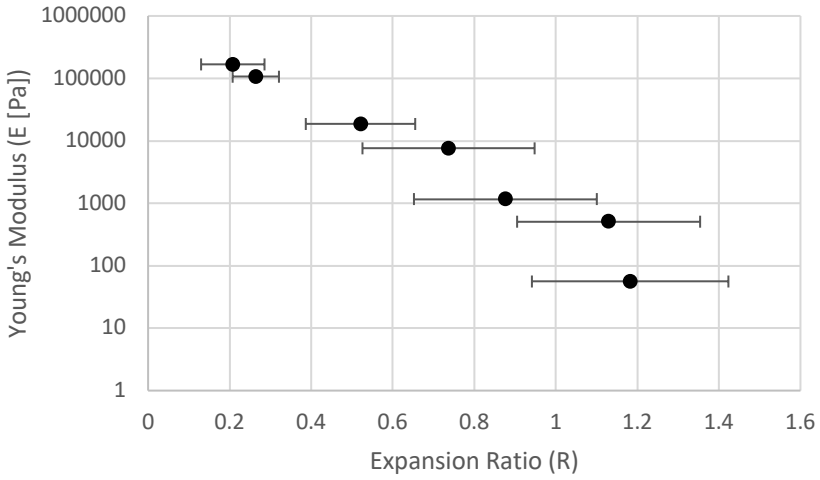

Figure 20: Sensor expansion ratio in matrices of varying stiffness. Error bars show standard deviation of sensor expansion ratio in each matrix stiffness.

We then converted the stiffness values to pressure values using the relation established previously and fit an exponential function to the data. This fit exponential function could then be input into the COMSOL model to act as the boundary load.

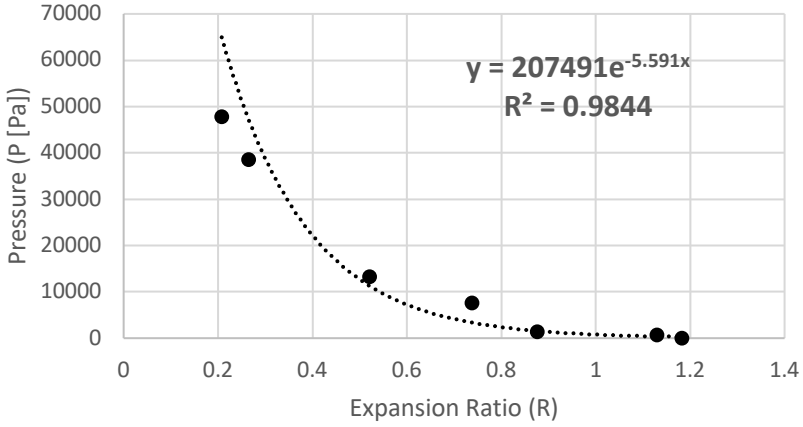

Figure 21: Stress-expansion ratio calibration curve and fit exponential function used as boundary pressure.

5.3 Stiffening and dissipation of viscous properties due to tissue fixation

To evaluate how these sensors could resolve viscous and elastic properties in tissues, we first wanted to demonstrate the ability of to distinguish linearly elastic materials from viscoelastic ones while staying within the confines of a tissue. This was achieved by evaluating both live and fixed T47D spheroids with fixation of tissues being known to stiffen tissues through the crosslinking of proteins and stabilization of the structure of cells. Spheroids were seed and imaged after 2 days to allow spheroids to aggregate. We then imaged sensors embedded in the spheroids with live video recordings of sensor expansion induced by adding PBS ice to wells.

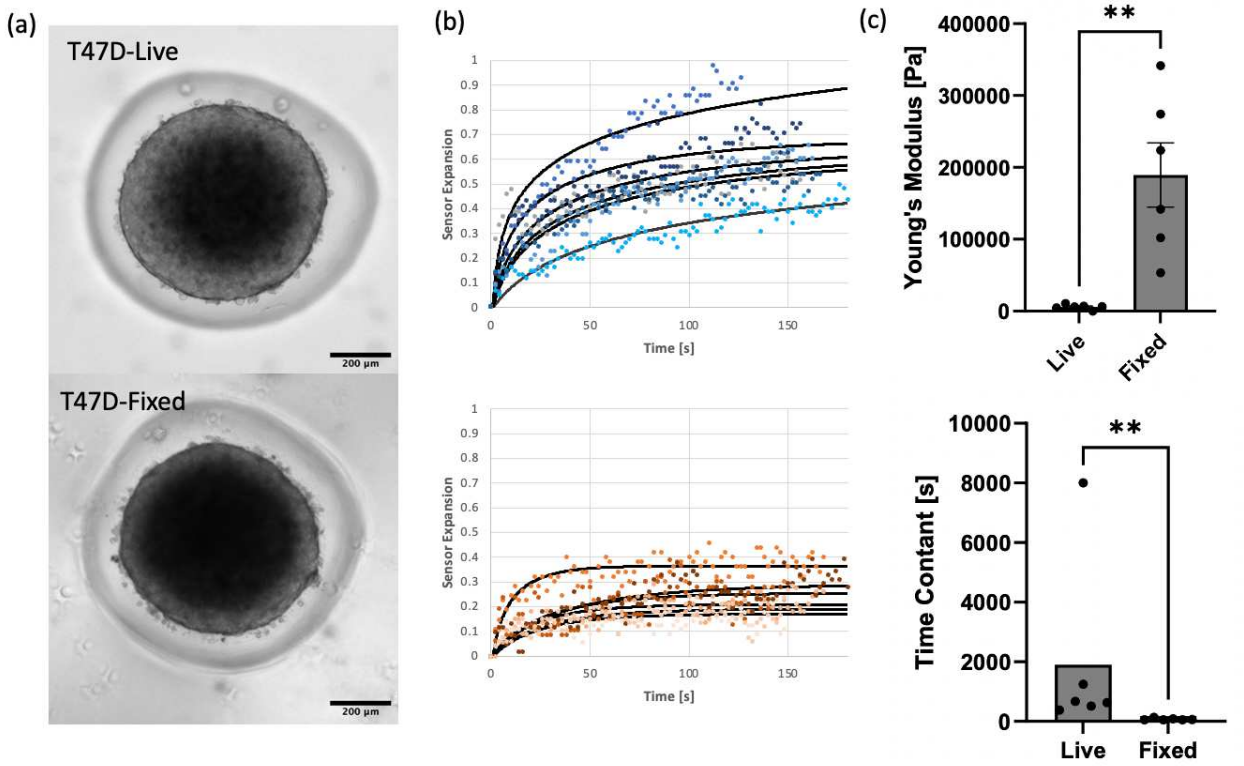

Figure 22: (a) Representative images of T47D spheroids pre and post fixation. (b) Sensor expansion profiles with corresponding modelled curves in live (top) and fixed (bottom) spheroids show vastly different shapes. (c) Measured Young's Modulus are significantly higher (n = 6, P<0.01 Mann-Whitney U-test) in fixed spheroids indicating stiffening due to fixation. Time constants in fixed spheroids are significantly lower in fixed tissues (n=6, P<0.01 Mann-Whitney U-test) indicating more linearly elastic response than live spheroids.

Unsurprisingly, the effect of protein cross-linking from fixation causes significant stiffening of the spheroids and dissipates any viscous properties making the tissue behave elastically.

5.4 Comparing viscoelasticity in spheroids from cell lines of distinct invasiveness

We then looked to see how viscoelasticity might vary between spheroids with invasive and non-invasive phenotypes and selected the highly invasive MDA-MB-231 breast cancer cell line to compare against the non-invasive T47Ds we had already tested. For these experiments, spheroids 500 μm in diameter we used as the dense nature of MDA-MB-231 spheroids caused size determination of sensors to be inaccurate due to extensive light diffraction throughout.

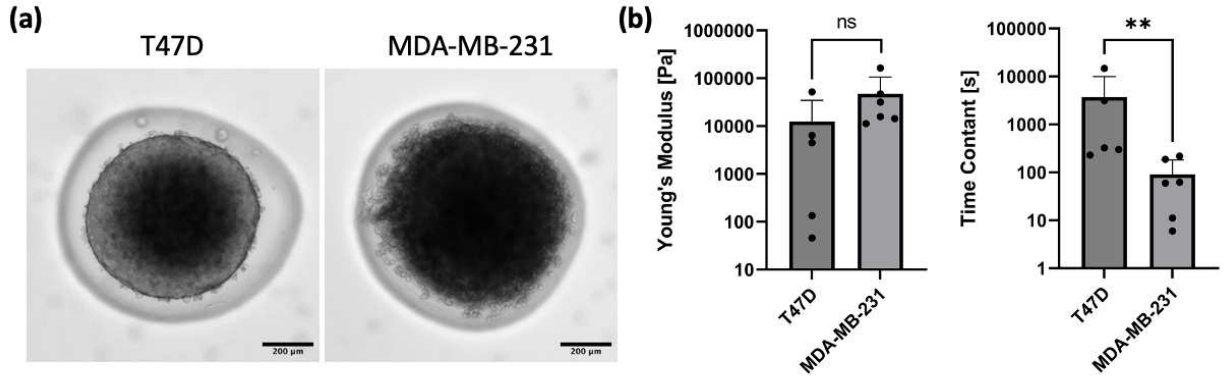

Figure 23: (a) Representative images of T47D and MDA-MB-231 spheroids show phenotypic differences with tight smooth boundary of T47Ds and a heterogenous rough edge of MDA-MB-231ss. (b) Measured Young's Modulus are not significantly different (Mann-Whitney U-test) between invasive and non-invasive spheroids. Time constants in invasive MDA-MB-231 spheroids are significantly lower than T47Ds indicating a dissipation of viscous properties (n=5-6, P<0.01 Mann-Whitney U-test).

Consistent with previous findings, the stiffness of invasive and non-invasive spheroids was not significantly different with substantial heterogeneity seen in both samples but more in the T47Ds. Importantly, there is a significant decrease in time constants in the invasive MDA-MB-231 spheroids which could prove to be a useful indicator for invasiveness with further investigation.

5.5 Evaluating local changes in viscoelasticity from induced invasive transitions

As a final test for the platform, we embedded sensors in spheroids with an inducible Src gene which has been demonstrated in invasion assays to greatly increase invasiveness when treated. Spheroids were again formed over but allowed to aggregate for 3 days. Sensors were then imaged without induction and the position of the observed sensors was recorded. We then treated the spheroids with complete media supplemented with 5 μg/ml of the antibiotic doxycycline and spheroids were left for 1 day for induction to take hold. We then returned to the previous sensors recorded initially and reimaged their expansion in the now treated spheroids.

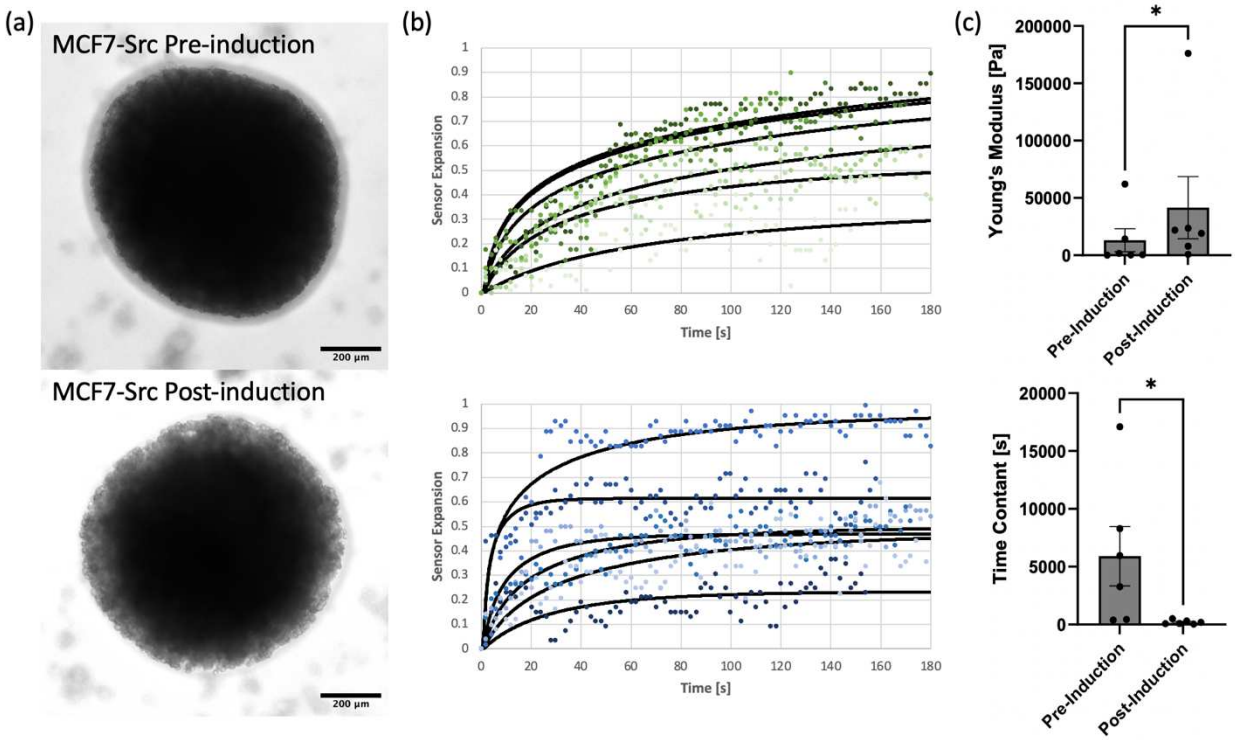

Figure 24: (a) Representative images of MCF7-Src spheroids pre and post induction. (b) Sensor expansion profiles with corresponding modelled sensor expansion curves before (top) and after (bottom) spheroid induction. (c) Measured Young's Modulus are significantly higher (n = 6, P<0.05 Wilcoxon signed-rank test) at the same location in induced spheroids indicating stiffening of the tissue. Time constants after induction are significantly lower (n=6, P<0.05 Wilcoxon signed-rank test) indicating more linearly elastic response.

The morphology of spheroids shows a drastic change over the 1 day of induction treatment with the pre-induction spheroid appearing similarly smooth and compact to the T47D spheroids while post-induction, the spheroids take on a similar morphology to the MDA-MB-231 spheroids.

Unlike the changes in viscoelasticity seen between T47Ds and MDA-MB-231s, all sensors showed local stiffening and a reduction of the time course of sensor expansion suggesting the induced invasiveness may also be causing stiffening of the tissue which is only evident by the repeated measures of viscoelasticity in the same location.

6. Discussion

6.1 Sensor calibration

When characterizing sensor stress, it was essential to cover the entire dynamic range of the sensors however due to the approach taken for measuring sensor stress based on surrounding matrix deformation, it becomes increasingly challenging to get an accurate estimation of stress near a zero-expansion ratio and nearing full sensor expansion. In theory, all materials deform under a load however our ability to measure that deformation quickly becomes the limiting factor, especially in the case of these sensors. In the highest stiffness polyacrylamide phantom which we could fabricate, we were still only able to constrain sensor expansion to 0.2 which meant that we were unable to inform our calibration curve of the levels of stress generated at very low expansion ratios. This is inconsequential for stiffness measurements as only the final equilibrated sensor expansion is used, and no tissue model has constrained sensors to such a low expansion ratio. With the time dynamic simulations for evaluating viscoelasticity however, we must model sensors as they transition from no expansion to their final expanded state which necessitates fitting a stress expansion ratio relation over the whole range. As a result, the initial stress applied on the model is an extrapolation of the calibration data we have collected but may not be truly indicative of the true stress generated by sensors.

To minimize error and improve convergence of the model over the first few seconds of the simulation, we employed a time ramp function which loads on the stress over the first 2 seconds with the intention of transitioning through to an expansion ratio and applied stress which has been properly characterized. To improve upon this process, we intend to make repeated

characterizations of sensor actuation in elastic matrices to better estimate the time dynamics of actuation at the start of the simulation. It would also be beneficial to use another linearly elastic matrix similar to polyacrylamide which can be tuned to even higher stiffnesses for characterizing stress at lower expansion ratios. Alginate gels could be an option for generating phantoms of very high stiffness which would likely be compatible with pNiPAAm sensors as they are hydrogels so the pNiPAAm can still quickly hydrate with water from the surrounding matrix.

We have also selected the Kelvin-Voigt model for viscoelasticity to better fit model sensor expansion profiles with those seen in experiment as the Kelvin-Voigt model does not allow instantaneous displacement which further minimizes the effect of such a high stress being applied at the very beginning of a simulation. With a more indicative ramp in based on actual sensor expansion in linearly elastic matrices, we may be able to use a more descriptive model for viscoelasticity such as the Standard Linear Solid model to better describe the sensor expansion profiles observed. It has become evident that a two-parameter model like the Kelvin-Voigt is helpful as the physical meaning of the parameters is very clear, but it does not always accurately simulate the longer constant viscous deformation that we sometimes see in the sensor deformation profiles. It is uncertain whether the added complexity of a more advanced viscoelastic model has much benefit as we've shown simple measures of the viscous properties can be a clear indicator of viscous differences and they are more easily analyzed and compared.

6.2 Model assumptions

With any model, there are assumptions that are made because not all aspects of the real world can be perfectly simulated.

All simulations used a Poisson ratio of 0.457 which was found in literature. While it is apparent that this value is not representative of all tissues, it is a reasonable approximation and the added complexity of modeling a dynamic Poisson ratio was deemed unnecessary . We have also seen that variation of the stress-strain relationship in our model due to changes in the Poisson ratio are relatively small which further supported our decision to keep the value constant. In the end, we prioritized having continuity between out linear elastic simulations for determining boundary pressure and viscoelastic simulations for measuring viscoelastic parameters.

6.3 Imaging Challenges

Much of the technical challenge of this work revolved around the imaging of sensors embedded in spheroids. While bead edge clarity was improved with the fluorescent particles loaded into sensors, there is still difficulty in penetrating light through dense tissues. With sensors randomly distributed throughout the spheroids, sensors were often at different depths within the tissue with deeper embedded sensors being far less clear than those near to the surface. Not much can be done to remedy this challenge without employing a different imaging modality, but few techniques have the speed required to image every few seconds at such a high resolution.

Adding to the challenge of imaging these sensors is the size change causes the focal plane of sensors to change which then requires live adjustment to maintain focus. Given the short timescale of sensor expansion, it is essential that accurate sensor size measurement is possible otherwise the data being fed into the model will not be representative of the true sensor expansion profiles.

Even further complicating imaging is how cold shocking of samples is achieved. By adding pieces of frozen PBS, we can quickly drop the temperature of the media with convection of the warm media and cold melting PBS adequately cooling sensors beyond the transition temperature for pNiPAAm. In doing so, there is further disruption and movement in the tissue which adds to the challenge of maintaining focus just as the sensor actuates.

6.4 Temperature control within tissues

As evidenced by the raw images of sensor expansion in tissues, the actuation of the sensors does not always occur at the onset of cooling, likely due to heat transfer limitations into the opening of micropocket devices and through the tissue. This further complicates analysis of sensor expansion as the onset is determined through when we visually see the sensor expand. Due to the small size of tissues used, we can be confident that sensors are adequately cooled and quickly expand but such delays add uncertainty to the imaging as sensors which shift out of focus appear to increase in size just as they do during sensor actuation.

There is also evidence in literature that the temperature of a tissue affects the mechanical properties of said tissue. In general, cooling a tissue will cause the stiffness to increase and the viscosity to decrease (resulting in decreased time constants) however the degree to which these changes may affect the tissues in this investigation are unclear[83,84]. In this study, the maximum temperature change in tissues is 37°C which overestimates the actual temperature drop of the tissue as samples remain in a heated on-stage incubator after cold shocking with ice. Over such a temperature range, the degree to which mechanical properties may change is unclear as no studies have evaluated this specific tissue type. While this mechanical change is potentially

present, all measurements are made under the same conditions and so the measured differences in mechanical properties between samples would still be present in uncooled tissues. In the previous work using these pNiPAAm sensors[14], samples were only cooled to room temperature through passive cooling however the range of stiffnesses observed in tissues of the same cell lines is in line with the values of Young's Modulus evaluated in this study of viscoelasticity. Despite a more aggressive cooling strategy which likely cools tissues well below room temperature, we do not see substantial changes in mechanical properties because of this change compared to this previous study.

6.5 Length of sensor expansion experiments

In many of our results, we observed sensor expansion in tissues where the creep behavior continues beyond the length of time which we had imaged. In theory, the model can resolve the difference in timescale observed as evidenced by the data presented however it is likely that the error of these measurements is substantially higher than those where sensor size plateaus. With the time-scale of viscous properties being established from this initial study, future use of sensors should track sensor size change for a longer time to better map the highly viscous regions of tissues which have been observed.

6.6 Changes in viscous properties of invasive tissues

As shown in comparing the viscoelastic properties of T47D spheroids to MDA-MB-231 spheroids, it is evident that there are distinct differences to the viscous properties which could be attributed to the difference in invasiveness between the tissues. This finding is a first step towards using local tissue viscoelasticity as an indicator for potential invasiveness which would be immensely

useful for diagnostics in breast cancer where an overtreatment of the disease is prevalent which can be very harmful for patients.

The morphology of the non-invasive T47D and invasive MDA-MB-231 spheroids could give hints as to why there are such differences in the viscous response of the tissues. With T47D spheroids being so tightly packed with a clear smooth edge, it could be that the tissues internally are also much more tightly packed with tight junctions between cells that therefor create slow viscous responses while the rougher boundaries of MDA-MB-231 spheroids could indicate more space between cells despite strong anchorage between cells which causes a loss in viscous properties.

While the inducible invasive model confirmed the dissipation in viscous properties in invasive tissues, we also observed local stiffening throughout the tissue with each sensor having smaller final expansion ratios then pre-induction. We hypothesize that this may not be representative of the invasive behavior of the tissue and may be caused by proliferation induced cell jamming. As visible in the representative images for MCF7-Src spheroids, the tissues fully fill the micropockets with very limited space between the edge of the tissue and the wall of the device. Given that induction greatly increases proliferation of cells, it is possible that the growth of the tissue results in compression of the spheroid which pushes the cells within the tissue together. This would cause the tissue to jam which would explain both the stiffening and elastic response observed in all sensors. This is especially evident because the sensors evaluated before and after induction are identical and we see that this change is consistent in all microregions tested.

If cell jamming is the cause, this type of platform would prove to be the first of its kind where a 3D tissue can be actuated to jam, analogous to tissues *in vitro* where the confinement of a tumor causes compression to accumulate and the cells within the tumor to jam.

7. Future Directions

The sensors adapted in this work for viscoelasticity have proven to be effective in distinguishing mechanical properties in breast cancer spheroids however mechanical properties are essential in all tissues in some form so adaptation of the sensors to other tissue platforms is the natural progression of the work. The use of these sensors as stiffness sensors has already begun with the investigation of breast cancer metastasis to multiple organs including the lung, liver, and brain. Likewise, sensors have been tested in engineered cartilage where the stiffness is on the top end of the range seen in breast cancer tumors but still within the dynamic range of the sensors. There is also potential for these sensors to sense anisotropic stiffness however only preliminary data which does not show consistent directional stiffness has been observed as of yet.

With all the above tissue models, the viscoelastic properties would be very relevant but due to the challenges in imaging sensor expansion, they have not been evaluated yet. With new imaging techniques being developed within the Moraes lab including a light sheet microscope and line scanning confocal microscope well adapted to the imaging needs of this work, there are plans for further studies of viscoelasticity once the new imaging modalities come online.

The findings in the inducible MCF7-Src model of an actuated jamming transition would be instrumental to understanding how tissue migration develops in 3D and therefor is planned to be investigated further.

It is evident that the viscous properties of tissues are instrumental, especially with cancer so a more detailed study into the longer time-scale viscous properties of tissues is being developed. While these sensors are appropriate for sensing the instantaneous viscous properties as sensed

by cells, it is well reported that cells are responsive to applied stress and properties such as their strength of attachment have been shown to be indicative of cancer invasiveness. Therefore, sensors which can apply a constant stress on tissues and slowly translate in space through the tissue are also being developed with the intention of furthering our understanding of the dynamic viscous response of tissues to applied stress.

8. Conclusion

In this work, the viscoelastic properties at the cell-scale have been resolved using thermally actuated expanding hydrogel sensors. By embedding sensors in polyacrylamide phantom gels, the stress generated throughout the expansion of a sensor is characterized by modelling sensor expansion in a linearly elastic matrix. With sensor generated stress characterized, an inverse finite element simulation in COMSOL Multiphysics is adapted to optimize the parameters for the Kelvin-Voigt model for viscoelasticity to fit experimentally determined sensor expansion profiles.

Sensors were then embedded in a range of breast cancer spheroid models. First, sensors were used to distinguish the viscous properties of a live tissue from the linearly elastic properties of a fixed tissue. We then looked at the differences in viscoelastic properties between non-invasive T47D spheroids and highly invasive MDA-MB-231 spheroids which showed no significant differences in the stiffness of tissues but a statistically significant dissipation of viscous properties in the invasive MDA-MB-231 spheroids.

We then looked to confirm this finding with a genetically engineered inducible MCF7-Src which confirmed the dissipation of viscous properties but also showed distinct local stiffening in all microregions. This observation could be a first indication of a platform for inducing cell jamming transitions in a 3D tissue.

Overall, the sensors developed have been successful in evaluated differences in viscoelastic properties in stiff tissues. This development is the first of its kind as no previous technique has been used to resolve local viscoelastic properties within dense tissues and does so with minimal auxiliary equipment aside from temperature controlled live imaging on a fluorescent microscope.

With such immense potential for using viscous properties in investigating tissue mechanics, these sensors provide a new tool for evaluating viscoelasticity in complex 3D tissues.

9. References

1. Chaudhuri, O. *et al.* Extracellular matrix stiffness and composition jointly regulate the induction of malignant phenotypes in mammary epithelium. *Nat. Mater.* **13**, 970–978 (2014).
2. Coughlin, M. F. *et al.* Cytoskeletal stiffness, friction, and fluidity of cancer cell lines with different metastatic potential. *Clin. Exp. Metastasis* **30**, 237–250 (2013).
3. Discher, D. E., Janmey, P. & Wang, Y. Tissue Cells Feel and Respond to the Stiffness of Their Substrate. *Science* **310**, 1139–1143 (2005).
4. Guimarães, C. F., Gasperini, L., Marques, A. P. & Reis, R. L. The stiffness of living tissues and its implications for tissue engineering. *Nat. Rev. Mater.* **5**, 351–370 (2020).
5. Li, C., Guan, G., Li, S., Huang, Z. & Wang, R. K. Evaluating elastic properties of heterogeneous soft tissue by surface acoustic waves detected by phase-sensitive optical coherence tomography. *J. Biomed. Opt.* **17**, 057002 (2012).
6. Holliday, D. L. & Speirs, V. Choosing the right cell line for breast cancer research. *Breast Cancer Res.* **13**, 215 (2011).
7. Alibert, C., Goud, B. & Manneville, J.-B. Are cancer cells really softer than normal cells? *Biol. Cell* **109**, 167–189 (2017).
8. Efremov, Y. M. *et al.* Mechanical properties of cell sheets and spheroids: the link between single cells and complex tissues. *Biophys. Rev.* **13**, 541–561 (2021).
9. Elosegui-Artola, A. *et al.* Matrix viscoelasticity controls spatiotemporal tissue organization. *Nat. Mater.* **22**, 117–127 (2023).
10. Nam, S., Lee, J., Brownfield, D. G. & Chaudhuri, O. Viscoplasticity Enables Mechanical Remodeling of Matrix by Cells. *Biophys. J.* **111**, 2296–2308 (2016).

11. Huang, D. *et al.* Viscoelasticity in natural tissues and engineered scaffolds for tissue reconstruction. *Acta Biomater.* **97**, 74–92 (2019).
12. Charbonier, F., Indana, D. & Chaudhuri, O. Tuning Viscoelasticity in Alginate Hydrogels for 3D Cell Culture Studies. *Curr. Protoc.* **1**, e124 (2021).
13. Chaudhuri, O. Viscoelastic hydrogels for 3D cell culture. *Biomater. Sci.* **5**, 1480–1490 (2017).
14. Mok, S. *et al.* Mapping cellular-scale internal mechanics in 3D tissues with thermally responsive hydrogel probes. *Nat. Commun.* **11**, 4757 (2020).
15. Vining, K. H. & Mooney, D. J. Mechanical forces direct stem cell behaviour in development and regeneration. *Nat. Rev. Mol. Cell Biol.* **18**, 728–742 (2017).
16. Engler, A. J., Sen, S., Sweeney, H. L. & Discher, D. E. Matrix elasticity directs stem cell lineage specification. *Cell* **126**, 677–689 (2006).
17. Yeung, T. *et al.* Effects of substrate stiffness on cell morphology, cytoskeletal structure, and adhesion. *Cell Motil. Cytoskeleton* **60**, 24–34 (2005).
18. Pelham, R. J. & Wang, Y. Cell locomotion and focal adhesions are regulated by substrate flexibility. *Proc. Natl. Acad. Sci.* **94**, 13661–13665 (1997).
19. Trappmann, B. & Chen, C. S. How cells sense extracellular matrix stiffness: a material's perspective. *Curr. Opin. Biotechnol.* **24**, 948–953 (2013).
20. Barriga, E. H. & Mayor, R. Adjustable viscoelasticity allows for efficient collective cell migration. *Semin. Cell Dev. Biol.* **93**, 55–68 (2019).
21. MacQueen, L. *et al.* Three-dimensional mechanical compression of biomaterials in a microfabricated bioreactor with on-chip strain sensors. *Proc. 16th Int. Conf. Miniaturized Syst. Chem. Life Sci. MicroTAS 2012* 1141–1143 (2012).

22. MacQueen, L., Chebotarev, O., Simmons, C. A. & Sun, Y. Miniaturized platform with on-chip strain sensors for compression testing of arrayed materials. *Lab. Chip* **12**, 4178–4184 (2012).
23. Brodland, G. W., Yang, J. & Sweny, J. Cellular interfacial and surface tensions determined from aggregate compression tests using a finite element model. *HFSP J.* **3**, 273–281 (2009).
24. Zhao, R., Boudou, T., Wang, W.-G., Chen, C. S. & Reich, D. H. Decoupling cell and matrix mechanics in engineered microtissues using magnetically actuated microcantilevers. *Adv. Mater. Deerfield Beach Fla* **25**, 1699–1705 (2013).
25. Baraniak, P. R. *et al.* Stiffening of human mesenchymal stem cell spheroid microenvironments induced by incorporation of gelatin microparticles. *J. Mech. Behav. Biomed. Mater.* **11**, 63–71 (2012).
26. Zhao, R., Boudou, T., Wang, W.-G., Chen, C. S. & Reich, D. H. Magnetic approaches to study collective three-dimensional cell mechanics in long-term cultures (invited). *J. Appl. Phys.* **115**, 172616 (2014).
27. Montel, F. *et al.* Stress Clamp Experiments on Multicellular Tumor Spheroids. *Phys. Rev. Lett.* **107**, 188102 (2011).
28. Leroux, C.-E., Palmier, J., Boccara, A. C., Cappello, G. & Monnier, S. Elastography of multicellular aggregates submitted to osmo-mechanical stress. *New J. Phys.* **17**, 073035 (2015).
29. Essmann, C. L. *et al.* Mechanical properties measured by atomic force microscopy define health biomarkers in ageing C. elegans. *Nat. Commun.* **11**, 1043 (2020).
30. Guevorkian, K., Colbert, M.-J., Durth, M., Dufour, S. & Brochard-Wyart, F. Aspiration of biological viscoelastic drops. *Phys. Rev. Lett.* **104**, 218101 (2010).

31. Haase, K. & Pelling, A. E. Investigating cell mechanics with atomic force microscopy. *J. R. Soc. Interface* **12**, 20140970 (2015).
32. Thomas, G., Burnham, N. A., Camesano, T. A. & Wen, Q. Measuring the Mechanical Properties of Living Cells Using Atomic Force Microscopy. *J. Vis. Exp. JoVE* 50497 (2013) doi:10.3791/50497.
33. Dixson, R., Orji, N., Misumi, I. & Dai, G. Spatial dimensions in atomic force microscopy: Instruments, effects, and measurements. *Ultramicroscopy* **194**, 199–214 (2018).
34. Beekmans, S. V., Emanuel, K. S., Smit, T. H. & Iannuzzi, D. Minimally Invasive Micro-Indentation: mapping tissue mechanics at the tip of an 18G needle. *Sci. Rep.* **7**, 11364 (2017).
35. Diez-Perez, A. *et al.* Microindentation for in vivo measurement of bone tissue mechanical properties in humans. *J. Bone Miner. Res. Off. J. Am. Soc. Bone Miner. Res.* **25**, 1877–1885 (2010).
36. Oyen, M. l. Nanoindentation of Biological and Biomimetic Materials. *Exp. Tech.* **37**, 73–87 (2013).
37. Ashrafi, H. & Shariyat, M. A Nano-indentation Identification Technique for Viscoelastic Constitutive Characteristics of Periodontal Ligaments. *J. Biomed. Phys. Eng.* **6**, 109–118 (2016).
38. Efremov, Y. M., Kotova, S. L. & Timashev, P. S. Viscoelasticity in simple indentation-cycle experiments: a computational study. *Sci. Rep.* **10**, 13302 (2020).
39. Boughton, O. R. *et al.* Measuring bone stiffness using spherical indentation. *PLoS ONE* **13**, e0200475 (2018).

40. Di Cerbo, A. *et al.* Mechanical phenotyping of K562 cells by the Micropipette Aspiration Technique allows identifying mechanical changes induced by drugs. *Sci. Rep.* **8**, 1219 (2018).
41. Hochmuth, R. M. Micropipette aspiration of living cells. *J. Biomech.* **33**, 15–22 (2000).
42. Theret, D. P., Levesque, M. J., Sato, M., Nerem, R. M. & Wheeler, L. T. The application of a homogeneous half-space model in the analysis of endothelial cell micropipette measurements. *J. Biomech. Eng.* **110**, 190–199 (1988).
43. Guo, Q., Park, S. & Ma, H. Microfluidic micropipette aspiration for measuring the deformability of single cells. *Lab. Chip* **12**, 2687–2695 (2012).
44. Pedersen, J. A. & Swartz, M. A. Mechanobiology in the Third Dimension. *Ann. Biomed. Eng.* **33**, 1469–1490 (2005).
45. Baker, B. M. & Chen, C. S. Deconstructing the third dimension – how 3D culture microenvironments alter cellular cues. *J. Cell Sci.* **125**, 3015–3024 (2012).
46. Mariappan, Y. K., Glaser, K. J. & Ehman, R. L. MAGNETIC RESONANCE ELASTOGRAPHY: A REVIEW. *Clin. Anat. N. Y. N* **23**, 497–511 (2010).
47. Ozturk, A., Grajo, J. R., Dhyani, M., Anthony, B. W. & Samir, A. E. PRINCIPLES OF ULTRASOUND ELASTOGRAPHY. *Abdom. Radiol. N. Y.* **43**, 773–785 (2018).
48. Sigrist, R. M. S., Liau, J., Kaffas, A. E., Chammas, M. C. & Willmann, J. K. Ultrasound Elastography: Review of Techniques and Clinical Applications. *Theranostics* **7**, 1303–1329 (2017).
49. Braun, J. *et al.* High-resolution mechanical imaging of the human brain by three-dimensional multifrequency magnetic resonance elastography at 7T. *NeuroImage* **90**, 308–314 (2014).

50. Streitberger, K.-J. *et al.* High-resolution mechanical imaging of glioblastoma by multifrequency magnetic resonance elastography. *PloS One* **9**, e110588 (2014).
51. Gandhi, D. *et al.* Magnetic resonance elastography-derived stiffness of the kidneys and its correlation with water perfusion. *NMR Biomed.* **33**, e4237 (2020).
52. Chan, R. C. *et al.* OCT-based arterial elastography: robust estimation exploiting tissue biomechanics. *Opt. Express* **12**, 4558–4572 (2004).
53. Huang, D. *et al.* Optical Coherence Tomography. *Science* **254**, 1178–1181 (1991).
54. Gillies, D. *et al.* Real-time and non-invasive measurements of cell mechanical behaviour with optical coherence phase microscopy. in 100670Y (2017). doi:10.1117/12.2251492.
55. Kennedy, K. M. *et al.* Quantitative micro-elastography: imaging of tissue elasticity using compression optical coherence elastography. *Sci. Rep.* **5**, 15538 (2015).
56. Serwane, F. *et al.* In vivo quantification of spatially varying mechanical properties in developing tissues. *Nat. Methods* **14**, 181–186 (2017).
57. Mongera, A. *et al.* Mechanics of the cellular microenvironment as probed by cells in vivo during zebrafish presomitic mesoderm differentiation. *Nat. Mater.* **22**, 135–143 (2023).
58. Roeder, R. K. Chapter 3 - Mechanical Characterization of Biomaterials. in *Characterization of Biomaterials* (eds. Bandyopadhyay, A. & Bose, S.) 49–104 (Academic Press, 2013). doi:10.1016/B978-0-12-415800-9.00003-6.
59. Mahoney, L. & Csima, A. Efficiency of palpation in clinical detection of breast cancer. *Can. Med. Assoc. J.* **127**, 729–730 (1982).
60. Agus, D. B. *et al.* A physical sciences network characterization of non-tumorigenic and metastatic cells. *Sci. Rep.* **3**, 1449 (2013).

61. Han, Y. L. *et al.* Cell swelling, softening and invasion in a three-dimensional breast cancer model. *Nat. Phys.* **16**, 101–108 (2020).
62. Acerbi, I. *et al.* Human Breast Cancer Invasion and Aggression Correlates with ECM Stiffening and Immune Cell Infiltration. *Integr. Biol. Quant. Biosci. Nano Macro* **7**, 1120–1134 (2015).
63. Jaiswal, D. *et al.* Stiffness analysis of 3D spheroids using microtweezers. *PLOS ONE* **12**, e0188346 (2017).
64. Chang, J. M. *et al.* Stiffness of tumours measured by shear-wave elastography correlated with subtypes of breast cancer. *Eur. Radiol.* **23**, 2450–2458 (2013).
65. Northcott, J. M., Dean, I. S., Mouw, J. K. & Weaver, V. M. Feeling Stress: The Mechanics of Cancer Progression and Aggression. *Front. Cell Dev. Biol.* **6**, 17 (2018).
66. Atia, L., Fredberg, J. J., Gov, N. S. & Pegoraro, A. F. Are cell jamming and unjamming essential in tissue development? *Cells Dev.* 203727 (2021) doi:10.1016/j.cdev.2021.203727.
67. Blauth, E., Kubitschke, H., Gottheil, P., Grosser, S. & Käs, J. A. Jamming in Embryogenesis and Cancer Progression. *Front. Phys.* **9**, (2021).
68. Cai, G. *et al.* Compressive stress drives adhesion-dependent unjamming transitions in breast cancer cell migration. 2022.04.30.490153 Preprint at https://doi.org/10.1101/2022.04.30.490153 (2022).
69. Kim, J. H. *et al.* Unjamming and collective migration in MCF10A breast cancer cell lines. *Biochem. Biophys. Res. Commun.* **521**, 706–715 (2020).
70. Gniewek, P., Schreck, C. F. & Hallatschek, O. Biomechanical Feedback Strengthens Jammed Cellular Packings. *Phys. Rev. Lett.* **122**, 208102 (2019).

71. Ilina, O. *et al.* Cell–cell adhesion and 3D matrix confinement determine jamming transitions in breast cancer invasion. *Nat. Cell Biol.* **22**, 1103–1115 (2020).
72. Campbell, B. E., Mok, S. & Moraes, C. In Situ Measurement of Intra-tumoral Tissue Rigidity. *Methods Mol. Biol. Clifton NJ* **2614**, 237–246 (2023).
73. Engler, A. J. *et al.* Myotubes differentiate optimally on substrates with tissue-like stiffness. *J. Cell Biol.* **166**, 877–887 (2004).
74. Tse, J. R. & Engler, A. J. Preparation of hydrogel substrates with tunable mechanical properties. *Curr. Protoc. Cell Biol.* **Chapter 10**, Unit 10.16 (2010).
75. Wang, Y.-L. & Pelham, R. J. [39] Preparation of a flexible, porous polyacrylamide substrate for mechanical studies of cultured cells. in *Methods in Enzymology* vol. 298 489–496 (Academic Press, 1998).
76. Lee, W. *et al.* Dispersible hydrogel force sensors reveal patterns of solid mechanical stress in multicellular spheroid cultures. *Nat. Commun.* **10**, 144 (2019).
77. Lee, W. *et al.* Ultrasoft edge-labelled hydrogel sensors reveal internal tissue stress patterns in invasive engineered tumors. *Biomaterials* **296**, 122073 (2023).
78. Ma, Z., Sagrillo-Fagundes, L., Mok, S., Vaillancourt, C. & Moraes, C. Mechanobiological regulation of placental trophoblast fusion and function through extracellular matrix rigidity. *Sci. Rep.* **10**, 5837 (2020).
79. Zhao, L., Mok, S. & Moraes, C. Micropocket hydrogel devices for all-in-one formation, assembly, and analysis of aggregate-based tissues. *Biofabrication* **11**, 045013 (2019).
80. Takigawa, T., Morino, Y., Urayama, K. & Masuda, T. Poisson's ratio of polyacrylamide (PAAm) gels. *Polym. Gels Netw.* **4**, 1–5 (1996).

81. Li, J., Illeperuma, W. R. K., Suo, Z. & Vlassak, J. J. Hybrid Hydrogels with Extremely High Stiffness and Toughness. *ACS Macro Lett.* **3**, 520–523 (2014).
82. Picu, R. C., Deogekar, S. & Islam, M. R. Poisson's Contraction and Fiber Kinematics in Tissue: Insight From Collagen Network Simulations. *J. Biomech. Eng.* **140**, 0210021–02100212 (2018).
83. Bianchi, L. *et al.* Thermophysical and mechanical properties of biological tissues as a function of temperature: a systematic literature review. *Int. J. Hyperthermia* **39**, 297–340 (2022).
84. Kiss, M. Z., Daniels, M. J. & Varghese, T. Investigation of temperature-dependent viscoelastic properties of thermal lesions in ex vivo animal liver tissue. *J. Biomech.* **42**, 959–966 (2009).